Deployment of a passive acoustic detection system for reactive collision avoidance in autonomous underwater vehicles

by

Oscar Alberto Viquez Rojas

S.B., Massachusetts Institute of Technology (2013)

Submitted to the Department of Mechanical Engineering
in partial fulfillment of the requirements for the degree of

Master of Science in Mechanical Engineering

at the

MASSACHUSETTS INSTITUTE OF TECHNOLOGY

June 2017

Author ..... Signature redacted ...
Department of Mechanical Engineering
May 10, 2017

Certified by ..... Signature redacted .....
Henrik Schmidt
Professor of Mechanical and Ocean Engineering
Thesis Supervisor

Accepted by ..... Signature redacted
Rohan Abeyaratne
Professor of Mechanical Engineering
Chairman, Committee on Graduate Students

Deployment of a passive acoustic detection system for reactive collision avoidance in autonomous underwater vehicles

by

Oscar Alberto Viquez Rojas

Submitted to the Department of Mechanical Engineering
on May 10, 2017, in partial fulfillment of the
requirements for the degree of
Master of Science in Mechanical Engineering

Abstract

The use of autonomous vehicles in air, land and water has grown in recent years, with increased attention given to heavily transited areas. For the case of autonomous underwater vehicles, these regions of interest include harbors and river basins where the risk of collision rapidly increases with the number of ships. This thesis presents a collision avoidance system based on passive acoustic sensing, which may be used to alert an AUV's autonomy software of the threat that an approaching vessel may represent in such shallow water environments. Experiments were conducted to collect and process data from static and vehicle-mounted hydrophone arrays, and preliminary measurements were post-processed using various signal smoothing and data-fitting techniques. Results were then compared with a mathematical model used to describe the expected sound propagation profile, to identify how the system was limited by disturbances in the test conditions, such as variable ship speed and bearing, with respect to the vehicle's frame of reference. The benefits and limitations of each data processing approach were identified, and are herein discussed through three separate case studies to highlight the benefit of parallel-model fitting. A Bluefin SandShark AUV was used for a series of deployments performed to test the vehicle's ability to change behaviors in response to approaching vessels that present a chance of collision, relying exclusively on this passive sensing system as the alarm trigger. During the final autonomous behavior-response experiments spanning six distinct deployments, a total of 21 successful alarm triggers were recorded in the vehicle logs, along with a cumulative 142 minutes of acoustic data.

Thesis Supervisor: Henrik Schmidt
Title: Professor of Mechanical and Ocean Engineering

Acknowledgments

First and foremost, I would like to thank my advisor, Prof. Henrik Schmidt, for granting me the opportunity and support to conduct this project.

I am also deeply grateful to Dr. Erin Fischell for all her advice and help.

I extend a big thank you to all my friends and colleagues in the Laboratory for Autonomous Marine Sensing Systems (LAMSS) at MIT. Without them, vehicle deployment days - and this work - would have been impossible.

A special thanks goes to my good friend, Alex Keesling, who's mathematical intuition is out of this world. Our conversations about math, physics and data processing always gave me a new perspective for my work.

Words simply aren't enough to express the gratitude I have for my parents and siblings, who have always given me their best wishes, their unwavering support and encouragement.

I would also like to thank Chris Murphy, Amy Underwood and their team at Bluefin Robotics. Their support was paramount to the success of operations with the SandShark AUV. I am likewise grateful to Craig Lawrence, Program Manager at the Strategic Technology Office of the Defense Advanced Research Projects Agency (DARPA), for his role in the donation of a Bluefin SandShark to MIT LAMSS for fundamental AUV research.

This work was supported by DARPA, the MIT Lincoln Laboratory, the Office of Naval Research (ONR) and Battelle.

Contents

List of Figures

1 Introduction

The use of autonomous vehicles in air, land and water has increased over the last few decades, for their ability to perform critical tasks in hazardous or remote environments. The advantages of airborne operations have become a matter of popular knowledge in the wake of a worldwide aviation industry and the recent rise of drones, while land-based autonomous activity is gaining ground in the view of the layman thanks to advances in the self-driving car industry. The marine subset of autonomous vehicles has similarly gained attention in recent years, with applications in oil spill mapping [5] and containment [4], environmental sensing and the observation of marine populations [6], in addition to military and defense needs [8].

The growth seen in marine robotics stems, in part, from advances in computer systems and vehicle technology. Historically, marine vehicles remained a part of a niche field, of interest predominantly for military and specialized ocean sciences applications, a trend often associated with the difference in cost of entry even beyond the merely monetary sense. Air and land are within reach of anyone who might wish to operate such vehicles; users can operate autonomous or semi-autonomous air and land vehicles as close as their own homes or backyards. Access to suitable bodies of water tends to be far more restrictive for those looking to operate one of the existing marine robotics platforms. While some small scale and low-cost remotely operated vehicle (ROV) designs, such as the OpenROV project, help lower the bar into aquatic experimentation, autonomous underwater vehicles (AUVs) have typically been larger vessels with higher cost of ownership and operation. However, recent improvements in computer hardware and sensing technologies have led companies in the field of marine robotics to the development of small-scale, lower-cost platforms such as the Bluefin SandShark [2], which aim to further facilitate entry for research and industry applications.

The emergence of lower-cost AUV platforms such as the SandShark arrives in time to meet an increased demand for systems of this kind. Some applications for

these smaller vehicles include monitoring of more accessible and often more heavily transited areas, such as river basins, littoral zones and harbors [1]. Beyond environmental and defense uses, these vehicles may serve research groups focused in subjects such as human-robot interaction (HRI); teams in the field have taken to the water, seeking to exploit the challenges posed by such environments to push their studies in team coordination and the psychological effects of HRI systems to the next level [9]. However, the nature of such an actively changing, shallow-water environment requires that AUVs operating in the area be capable of responding to the presence of unknown ships to avoid possible collision scenarios. Furthermore, the limitations of underwater communications, and the variability of equipment and resources onboard the third-party vessels involved, calls for a system capable of alerting the AUV of potential threats without the need for two-way communication or pre-established identifying signatures.

This thesis expands on the subject of collision avoidance for AUVs by using a passive acoustic system fully contained onboard an unmanned vehicle, and pairing the sensor system with online processing to trigger behavioral responses in the autonomy middleware managing the active mission. The system is based on the algorithm presented by Prof. Henrik Schmidt and Dr. Michael Benjamin under project name ALPACA[1] [10, 11], and extends prior work on algorithm validation [13]. The system has been adapted for discretized sampling time windows and live data processing during mission deployments, considering various signal filtering solutions. Field tests were performed with ground-fixed and AUV-mounted hydrophone arrays, and collision avoidance behaviors were successfully triggered onboard the AUV in response to approaching motorized vessels during autonomous mission deployments.

[1]The ALPACA technology is owned by MIT. A patent has been issued under United States of America Serial No. 8830793, "System And Method For Collision Avoidance In Underwater Vehicles" by Henrik Schmidt and Michael Richard Benjamin. Patent issued on September 9, 2014.

2 Background

2.1 Acoustics

A study of acoustics typically begins with discussion of a case most readers can relate to: the sound produced by string instruments such as guitars or pianos. Drawing from the perception of sound coming from such an instrument, and the visual aid of the string's motion, this approach provides a baseline upon which an understanding of waves can be built [7]. From the mathematical description of string vibration as waves, the discussion advances to observing pressure waves in a medium. In order to properly describe these pressure fluctuations, the principles of conservation of mass and conservation of momentum are used to derive the wave equation. For an ideal fluid with coupled density and pressure, the adiabatic relation between these terms must also be considered in the derivation [3]. As explained in Section 2.1.2 of [3], "[t]he linear approximations, which lead to the acoustic wave equation, involve retaining only first-order terms in the hydrodynamic equations."

The wave equation may be expressed in different forms to solve for the pressure field, particle velocity, the velocity potential or displacement potential. Furthermore, the time-domain wave equation may be transformed into the Helmholtz equation, in frequency-domain, by using the corresponding frequency-time Fourier transform pair. Eq. 2.1 and 2.2 show the solutions to the Helmholtz equation in a homogeneous medium, for the cases of a plane wave and an omnidirectional point source respectively.

$$\psi(x,y,z) = \begin{cases} Ae^{i\mathbf{k}\cdot\mathbf{r}} \\ Be^{-i\mathbf{k}\cdot\mathbf{r}} \end{cases} \tag{2.1}$$

$$\psi(r) = \begin{cases} (A/r)e^{i\mathbf{k}\cdot\mathbf{r}} \\ (B/r)e^{-i\mathbf{k}\cdot\mathbf{r}} \end{cases} \tag{2.2}$$

In acoustics, quantities are most often expressed in decibels (dB), a ratio of two values expressed in terms of a base-10 logarithmic scale. It is for this reason that the sonar equation takes its form in the dB scale, where a given acoustic field can generally be expressed as separate additive terms with respect to reference values and length scales, such that the effect of aspects such as range from a source on the perceived amplitude at a receiver location may be treated separately. Reducing the system to an ideal scenario with no noise, the simple sonar equation can be expressed as Eq. 2.3, where L_p is the sound pressure level at a given receiver location, L_s is the source level, and TL is the transmission loss. This simplified form constitutes the foundation for the mathematical model (Sec. 3) upon which the present work is based. For additional information on the sonar equation, the reader may refer to Chapter 10, Section 10.2.2 of [3].

$$L_p = L_s - TL \tag{2.3}$$

2.1.1 Useful dB-scale expressions

The following are some useful expressions used in acoustics, based on the dB scale (Eq. 2.4). The sound pressure level L_p, used in the sonar equation as given in Eq. 2.3, relates the pressure p at a receiver location, to a reference pressure p_{ref}. Similarly, the power level L_W expresses the power W of a given source with respect to a reference power W_{ref}. The power level L_W and source level L_s are related to each other by a function of the reference terms.

$$\begin{aligned} L_p &= 10\log_{10}\left(\frac{|p|^2}{|p_{\text{ref}}|^2}\right) && \text{dB re } p_{\text{ref}} \\ L_W &= 10\log\left(\frac{W}{W_{\text{ref}}}\right) && \text{dB re } W_{\text{ref}} \\ L_W &= L_s + 10\log\left(\frac{p_{\text{ref}}^2 r_{\text{ref}}^2 4\pi}{W_{\text{ref}}\rho_0 c}\right) && \text{dB re } W_{\text{ref}} \end{aligned} \tag{2.4}$$

Parameters like the medium density ρ_0 and the speed of sound c vary across different fluid media. The reference pressure p_{ref} also differs for different fluids. Eq. 2.5 provides the typical values for the reference parameters used above.

$$
\begin{aligned}
W_{\text{ref}} &= 1\text{W} \\
r_{\text{ref}} &= 1\text{m} \\
p_{\text{ref}} &= \begin{cases} 1\mu\text{Pa, water} \\ 20\mu\text{Pa, air} \end{cases}
\end{aligned}
\tag{2.5}
$$

The expressions relating the intensity I and power W with the root mean square (RMS) of the pressure, expressed as $|p|$, and the acoustic impedance, given as the product $\rho_0 c$, are also used throughout this work (Eq. 2.6).

$$
\begin{aligned}
I &= \frac{|p|^2}{\rho_0 c} \\
I &= \frac{W}{Area}
\end{aligned}
\tag{2.6}
$$

3 Mathematical Model

As mentioned in Sec. 2.1, the model implemented in this thesis stems from the simple sonar equation (Eq. 2.3, revisited in Eq. 3.1), where L_p is the sound pressure level, L_s is the source level, and TL represents the transmission loss. For the cases of ideal spherical and cylindrical spreading, the transmission loss is given by Eq. 3.2, as a function of range r from the source.

$$L_p = L_s - TL \tag{3.1}$$

$$TL = \begin{cases} 20\log_{10}\frac{r}{r_{\text{ref}}}, & \text{spherical spreading} \\ 10\log_{10}\frac{r}{r_{\text{ref}}}, & \text{cylindrical spreading} \end{cases} \tag{3.2}$$

Because this project focuses on the use of AUVs in shallow-water environments (such as littoral areas, harbors and river basins), the assumptions and simplifications used in the field of ocean acoustics for this type of setting are used to further define the mathematical model.

3.1 Propagation Model for Shallow Water

The propagation of acoustic waves in shallow-water environments is principally affected by two defining characteristics. First, the sound speed profile in the water column is typically downward-refracting or near-constant, which means that for long-range propagation, most paths will likely involve boundary interactions (particularly, bottom interactions). Second, the properties of the boundary layers are spatially varying, and generally difficult to characterize with sufficient detail to enable long-range predictions. These properties of shallow-water acoustics aren't without merit, however, as "transmission is generally better than free-field propagation ($20\log r$) at short and intermediate ranges [...]" [3]. In these shorter ranges, the transmission loss is better described by cylindrical spreading, rather than spherical propagation.

3.2 ALPACA Intercept-Time Estimation

Expressing the simple sonar equation in terms of intensities, Eq. 3.1 becomes Eq. 3.3. This expression assumes cylindrical spreading, per the forms given in Eq. 3.2. The term I_0 represents the source intensity in dB, and I_{dB} represents the intensity observed by a receiver at a given range r from the source, in the same logarithmic scale.

$$\begin{aligned} I_{dB} &= I_0 - TL \\ &= I_0 - 10\log_{10}(r) \\ &= I_0 - \tfrac{10\log(r)}{\log(10)} \end{aligned} \tag{3.3}$$

As explained in [10, 11, 13], the core of the Autonomous Littoral Passive Acoustic Collision Alarm (ALPACA) system and method is based on this relationship between the acoustic intensity and the range-dependent transmission loss. While the corresponding range r and source level constant I_0 might not be known, the time-derivative of the measurements taken by a receiver (Eq. 3.4) can nonetheless be related to the intercept time dT (Eq. 3.5).

$$\begin{aligned} \Delta &= \tfrac{dI_{dB}}{dt} \\ &= \tfrac{\partial I_{dB}}{\partial r}\tfrac{dr}{dt} \\ &= -v * \tfrac{\partial I_{dB}}{\partial r} \\ &= \tfrac{10v}{\log(10)r} \end{aligned} \tag{3.4}$$

$$dT = \frac{r}{v} = \frac{10}{\log(10)\Delta} \tag{3.5}$$

3.3 Ideal Model Representation

This section provides a sample case based on the mathematical model described above, in order to introduce the data visualization tools used in later sections of this work.

For a source, selected such that the source intensity level is equal to the corresponding reference intensity (that is, $I_0 = 0$), the receiver intensity I_{dB} can be equated to the transmission loss directly. Fig. 3-1 shows the corresponding intensity

field for a 100m by 100m square grid, where the source is located at the origin. The intensity values are then plotted for ranges of 1m and greater, where $TL_{(r=r_{\text{ref}})} = 0$ and otherwise vary based on cylindrical propagation.

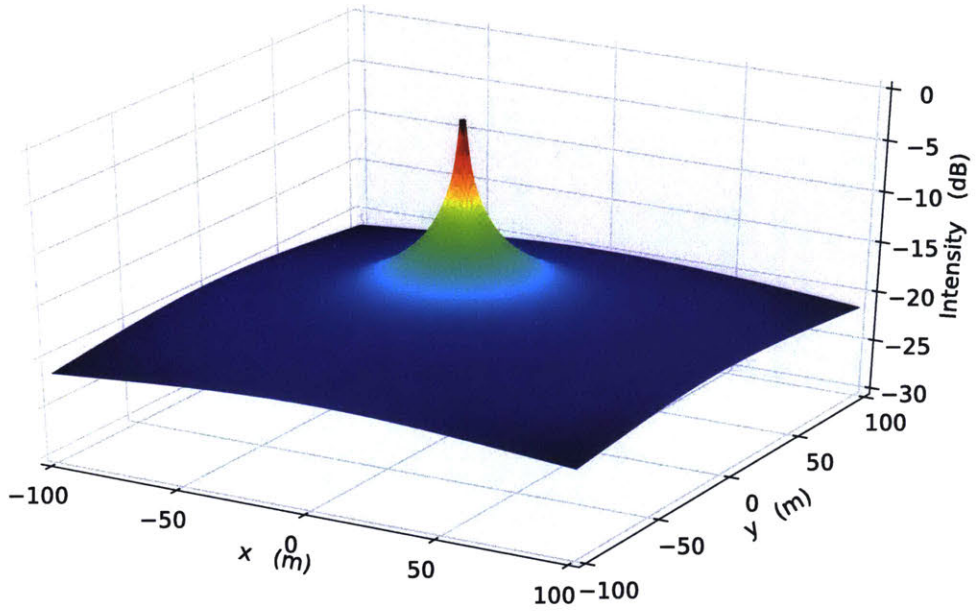

Figure 3-1: Intensity field in a 100m by 100m grid, based on cylindrical propagation. This form highlights the behavior of the source as a mathematical singularity.

The ALPACA intercept-time estimation is based on the correlation between time, acoustic intensity and the range between a source and the receiver. To better understand the profiles expected for the experimentation stage, and the effect of spatial offsets on the sensor data, consider the assumption of a ship traveling at constant speed along three straight travel lanes: one on a direct radial path over the AUV, and two others with different offsets from the radial path at their closest point of approach to the autonomous vehicle. This can be equally expressed as moving the AUV or receiver along the paths defined by $x = [0, 10, 20]$m, $y = 0$m, on the grid shown in Fig. 3-1. The intensities recorded by the sensor system would then be as shown in Fig. 3-2, with respect to the sensor's position along the x-axis.

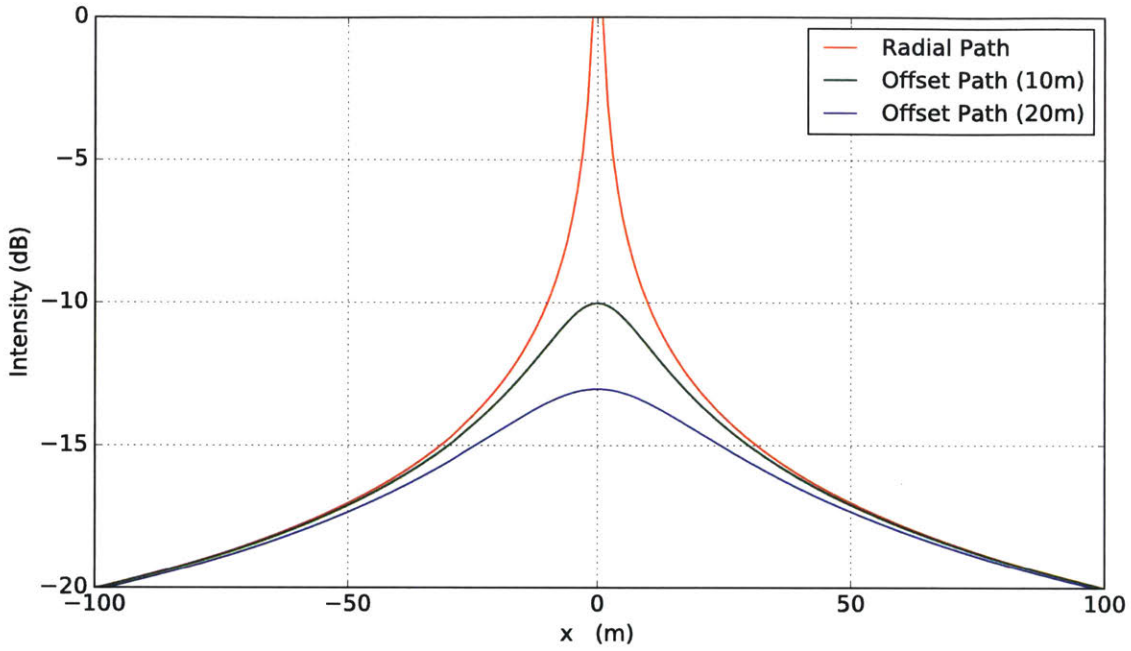

Figure 3-2: Intensity along 3 straight travel lanes in a 100m by 100m grid, with different offsets from the source at the closest point of approach.

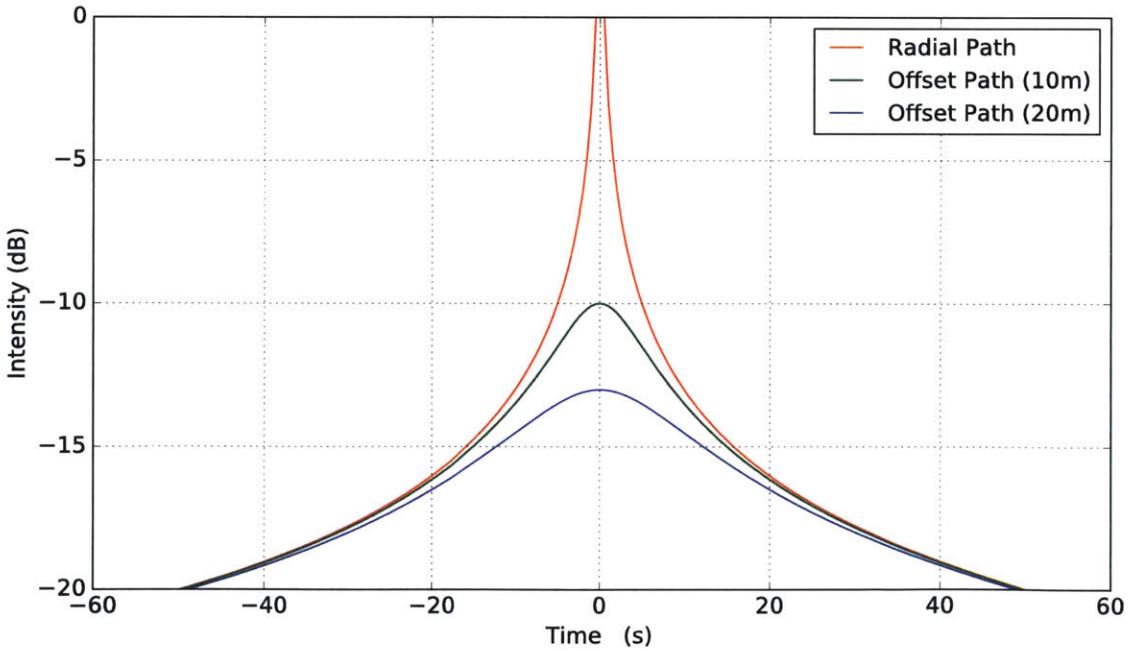

Figure 3-3: Intensity along 3 straight travel lanes with different offsets at the closest point of approach, for a constant ship speed of $v = 2\text{m/s}$.

Using the Cartesian XY plane to build this example scenario is a sensible choice to start from, as it preserves the spatial meaning of range-dependent propagation. However, the relative range will be unknown to the receiver in the system during real deployment; this is, in fact, one of the underlying motivations for using this passive acoustic detection method. By converting the data using a constant velocity v, the intensity values can then be expressed as will be perceived by the vehicle, with respect to time (Fig. 3-3).

The transformation of observed intensities in this model to time-domain is a necessary step to proceed with the ALPACA algorithm, as Eq. 3.4 calls for the time-derivative of the measurements. From there, it may be remarked that the behavior of the intensity differential around the singularity, at $t = 0$, is of particular importance given the reciprocal relation between Δ and the intercept time dT. Fig. 3-4 shows how even a small offset at the closest point of approach will allow for a smooth function in the derivative space, while a direct path model over the source will peak due to the singularity.

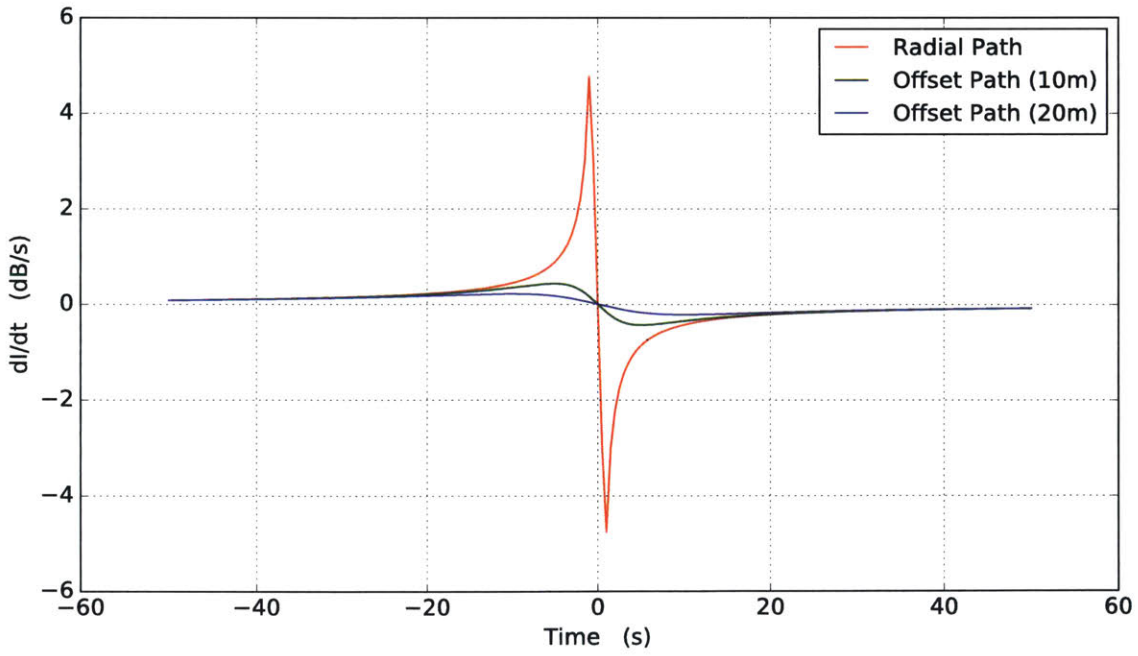

Figure 3-4: Gradient of intensity versus time, for a ship moving along 3 straight travel lanes with distinct offsets at their closest range.

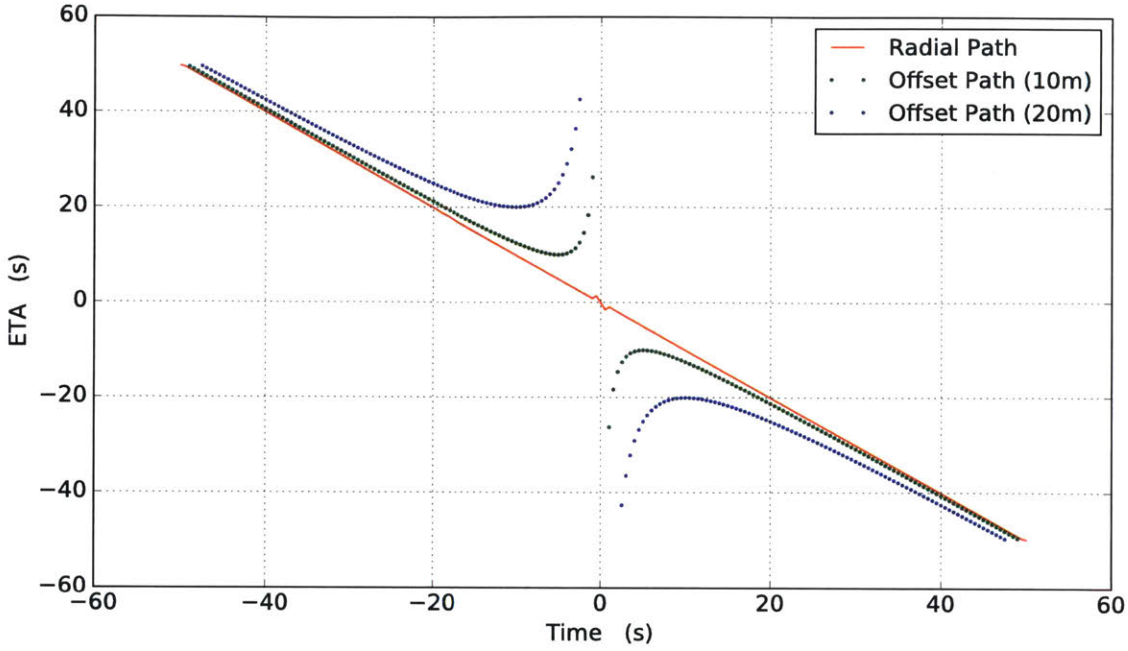

Figure 3-5: Estimated intercept time, for a ship moving along 3 straight travel lanes with different offsets from the source at their closest range.

Feeding the gradient results to Eq. 3.5 yields the estimated intercept time, as shown in Fig. 3-5. Here, it may be observed how the behavior of the singularity changes with the transformation from derivative space into intercept-time estimates. Where a slight offset from the source led to smooth functions in the intensity measurement and differential forms, the same shift translates to a discontinuity in estimated-time space.

3.4 Effect of Noisy Signal on ALPACA

During experimentation, the system will be susceptible to multiple sources of noise. From the disturbance introduced due to sensor error, to the effect of electronics and voltage fluctuations, and ever more so all the acoustic noise sources to be encountered during deployment, no two sets of measurements will likely be the same. Furthermore, the dependence of the algorithm on the derivative of the measurements and the reciprocal relation presented in Section 3.3 mean that understanding the effect

of noise in the algorithm makes an important part of the implementation process, to enable decision-making and to trigger behaviors during vehicle operations. Fig. 3-6 shows the radial-path signal presented earlier, along with a simulation of noisy measurements for the same scenario. The noise shown here is modeled as Gaussian, with a standard deviation of $\sigma = 0.001$, in the absolute intensity space. Note that units here are driven by the reference intensity I_{ref}; using a reference magnitude of I_{ref} =1W/m^2 sets these same units for the magnitudes shown in Fig. 3-6. Using the logarithmic relationship, Fig. 3-7 presents the same pair of signals in the decibel scale.

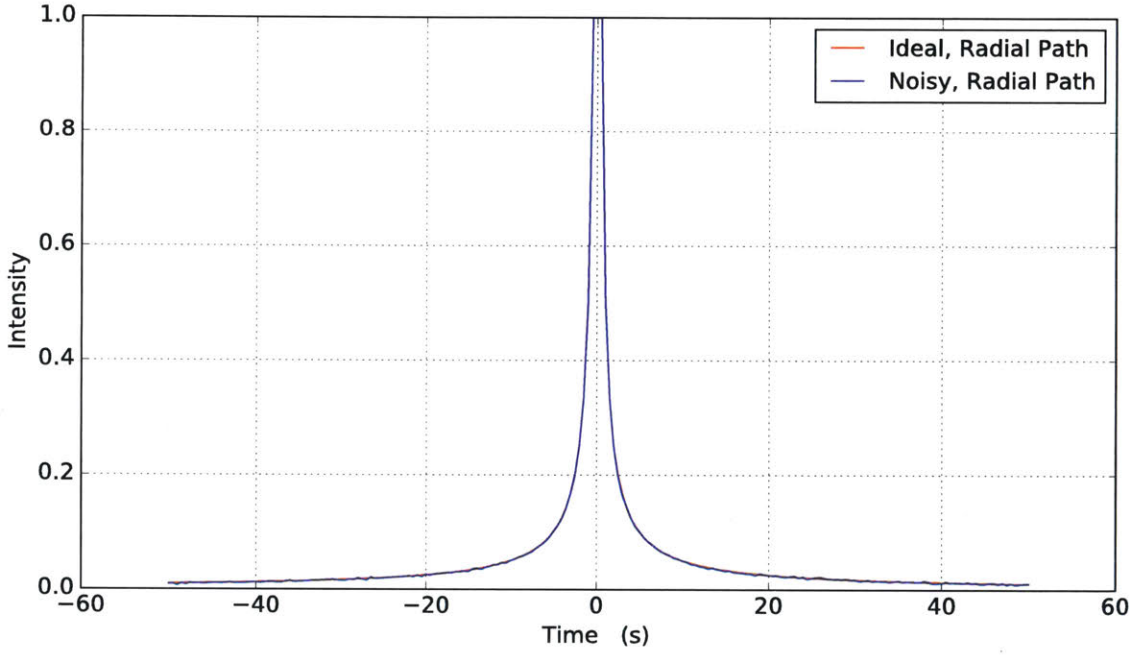

Figure 3-6: Intensity along a radial path of approach. Noisy signal simulated as Gaussian, with $\sigma = 0.001$.

As explained in Section 3.2, the intercept-time estimation system depends on the time-derivative of the intensity measurements. Given this mathematical relation, the effect of noise in the intensity signal may be amplified when using a point-to-point difference method to compute the gradient. Such a method may noticeably affect the performance of the algorithm, as shown in Figs. 3-8 and 3-9. Section 5.1.1 discusses various methods used to address this issue.

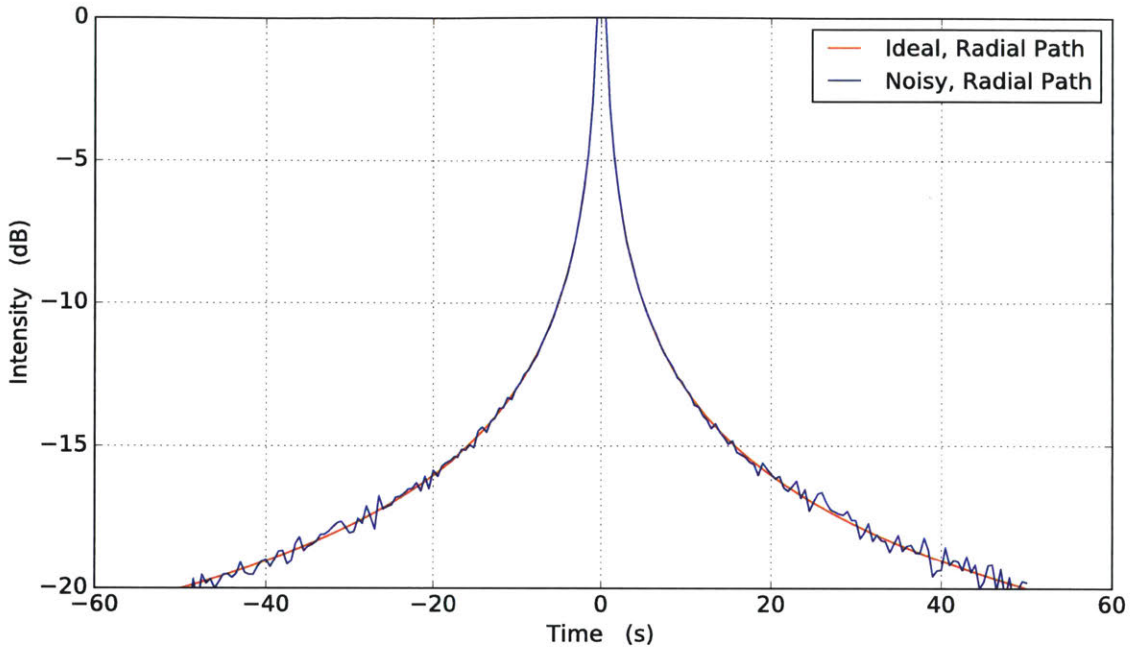

Figure 3-7: Intensity (dB) along a radial path of approach. Noisy signal simulated as Gaussian in the absolute intensity space, with $\sigma = 0.001$.

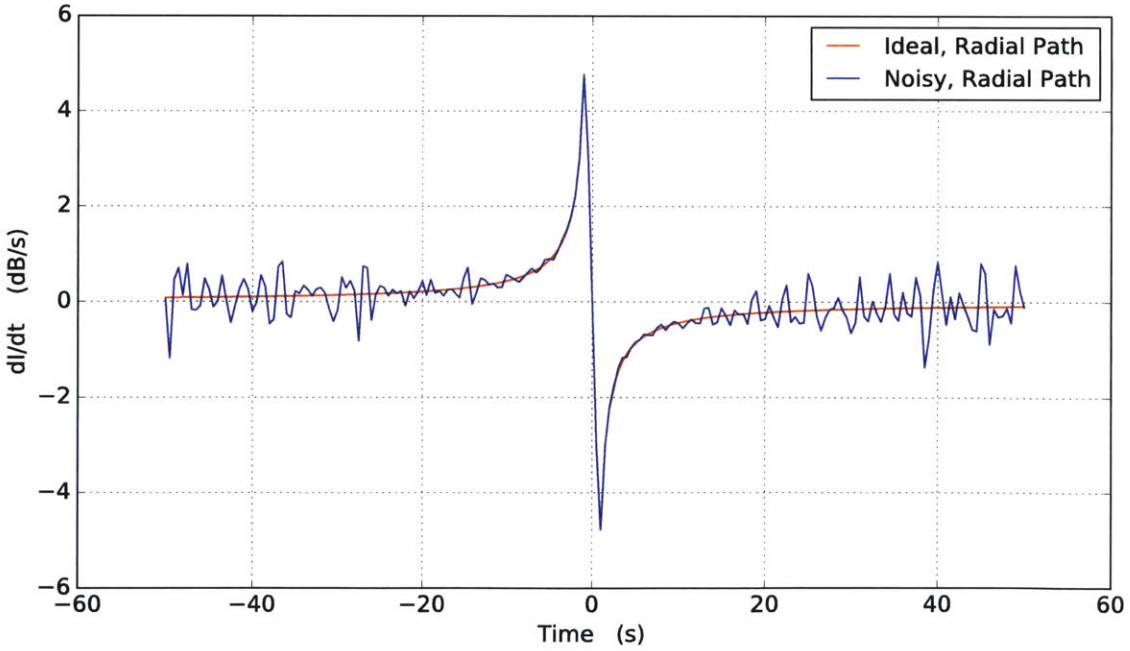

Figure 3-8: Gradient of intensity versus time, comparing ideal and noisy signals.

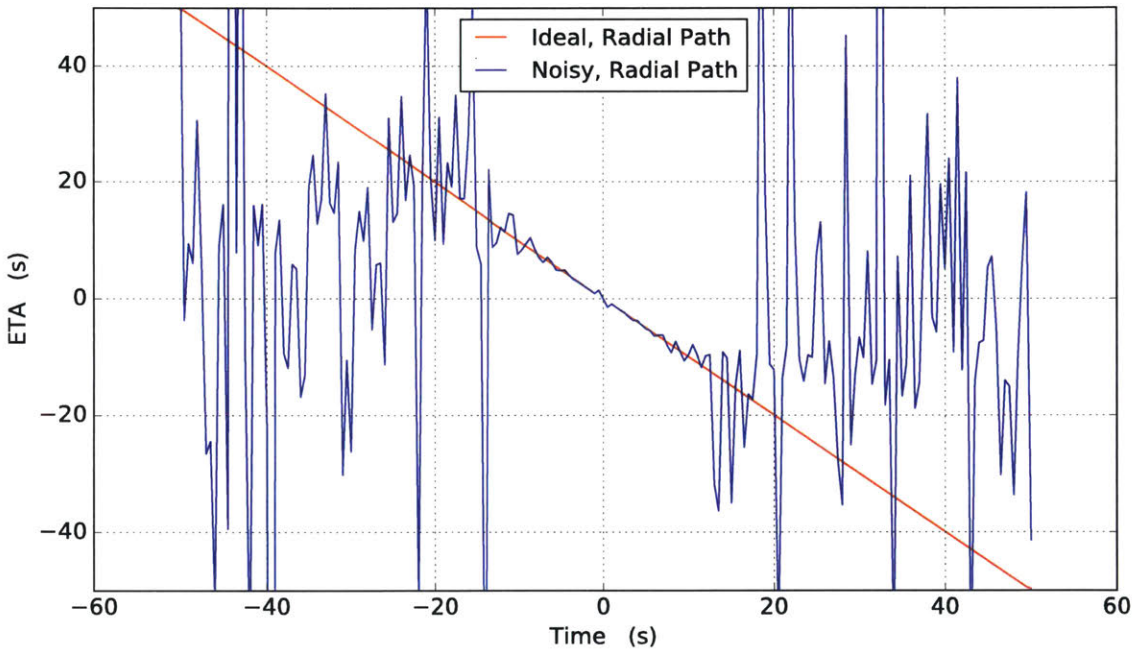

Figure 3-9: Estimated intercept time for a radial path of approach, comparing ideal and noisy signals.

3.5 Pressure Form of ALPACA

As part of this work, an alternate form has been derived to express the intercept-time estimation from pressure values, in place of intensity measurements. This approach stems from the nature of the sensors used, as the hydrophones output a voltage signal proportional to pressure, and relies on the acoustic impedance relation provided in Eq. 2.6. Assuming a constant acoustic impedance $\rho_0 c$, the derivation follows from Eq. 3.6 as shown in Eq. 3.7 to relate pressure and range. The intensity I_{dB} at the receiver has been renamed as the measured intensity I_m, given in the decibel scale. Figs. 3-10 and 3-11 show how the pressure and intensity magnitudes relate, normalized by the constant scaling factor $\rho_0 c$.

$$I_m = I_0 - \frac{10\log(r)}{\log(10)} \tag{3.6}$$

$$\begin{aligned} I_0 - I_m = 10\log_{10}\left(\frac{|p_0|^2}{\rho_0 c}/\frac{|p_m|^2}{\rho_0 c}\right) &= 20\log_{10}\left(\frac{|p_0|}{|p_m|}\right) = \frac{10\log(r)}{\log(10)} \\ \log_{10}(|p_m|) - \log_{10}(|p_0|) &= \frac{\log(|p_m|)}{\log(10)} - \frac{\log(|p_0|)}{\log(10)} = -\frac{1}{2}\frac{\log(r)}{\log(10)} \\ \log(|p_m|) - \log(|p_0|) &= -\frac{1}{2}\log(r) \end{aligned} \tag{3.7}$$

Taking the derivative yields Eq. 3.8 (Figs. 3-12 and 3-13).

$$\begin{aligned} \frac{d}{dt}\left(\log(|p_m|) - \log(|p_0|)\right) &= -\frac{1}{2}\frac{1}{r}\frac{dr}{dt} \\ \frac{1}{p_m}\frac{dp_m}{dt} &= \frac{1}{2}\frac{1}{r}v \\ \frac{r}{v} &= \frac{1}{2}\frac{p_m}{p'_m} \end{aligned} \tag{3.8}$$

The intercept time dT can then be expressed in terms of the pressure as shown in Eq. 3.9 (Figs. 3-14 and 3-15). The intercept times for both ideal and noisy signals are a match between the intensity and pressure forms, up to a small rounding error.

$$dT = \frac{1}{2}\frac{p_m}{p'_m} \tag{3.9}$$

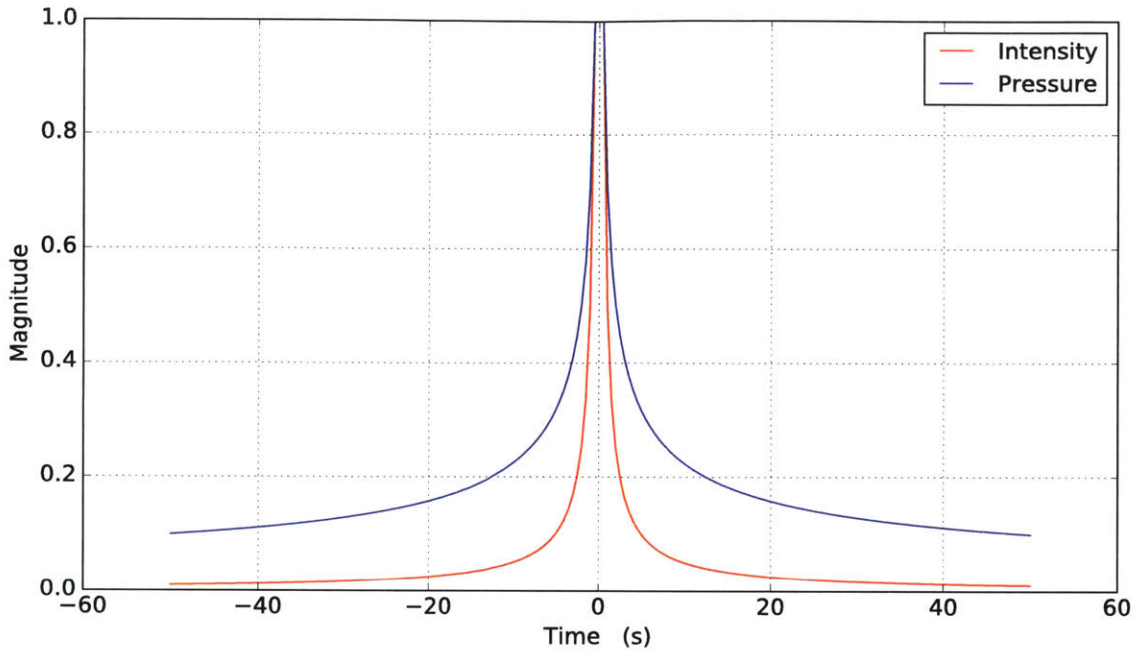

Figure 3-10: Magnitudes of intensity and pressure along a radial path of approach, to a constant $\rho_0 c$.

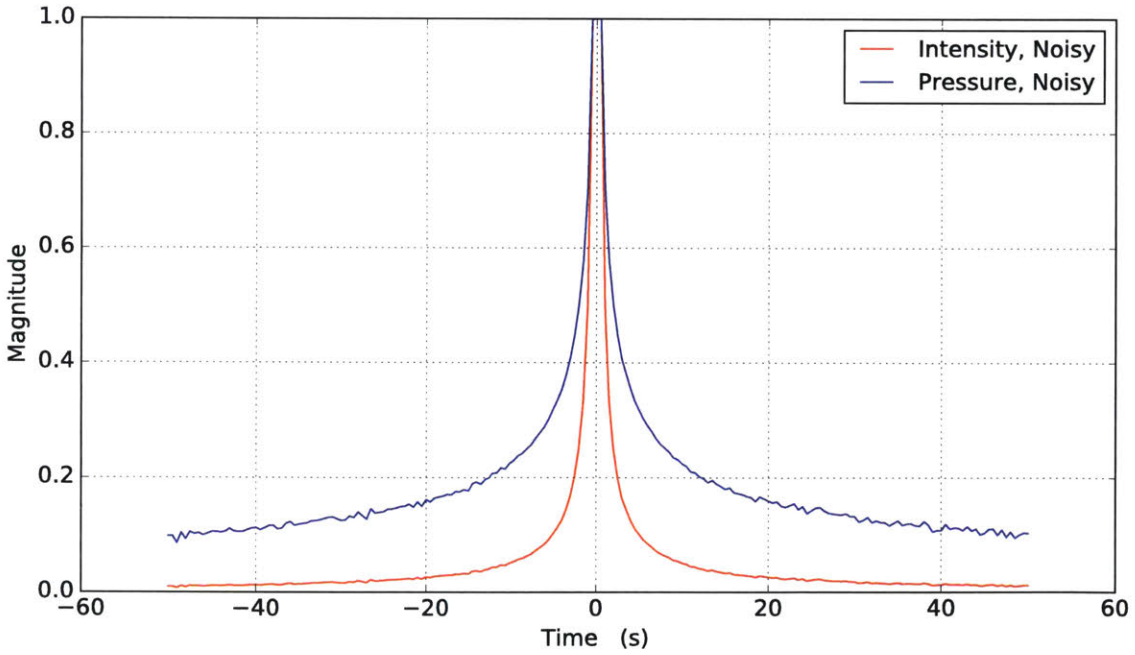

Figure 3-11: Magnitudes of intensity and pressure along a radial path of approach, to a constant $\rho_0 c$. Noisy signal simulated as Gaussian, with $\sigma = 0.001$.

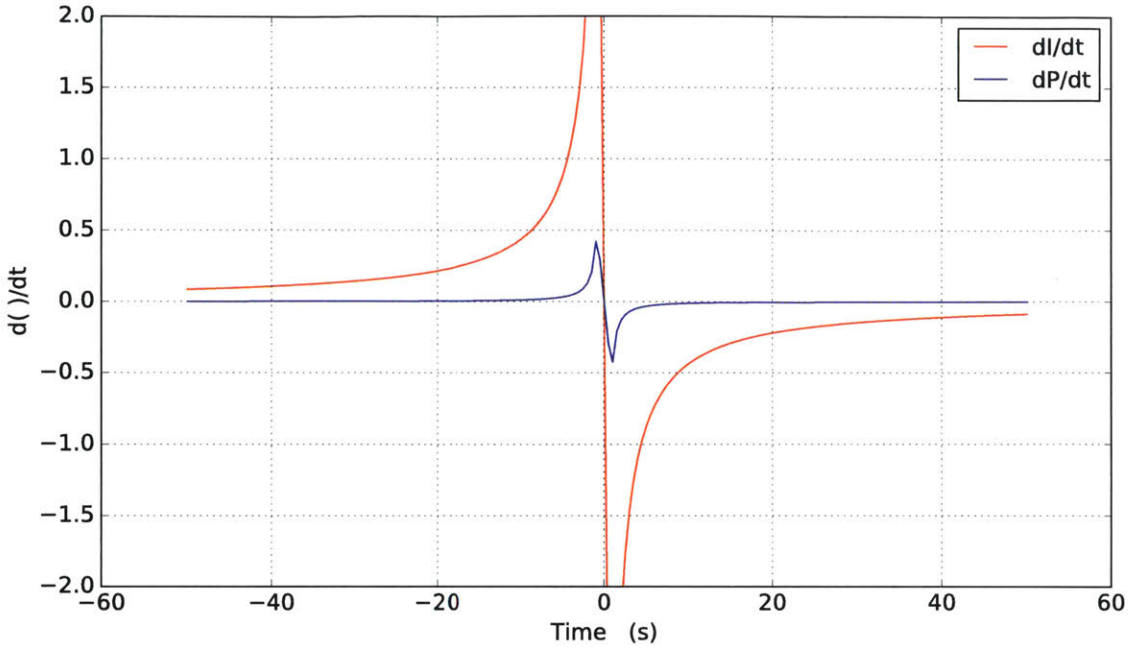

Figure 3-12: Gradient of intensity and pressure versus time, along a radial path of approach.

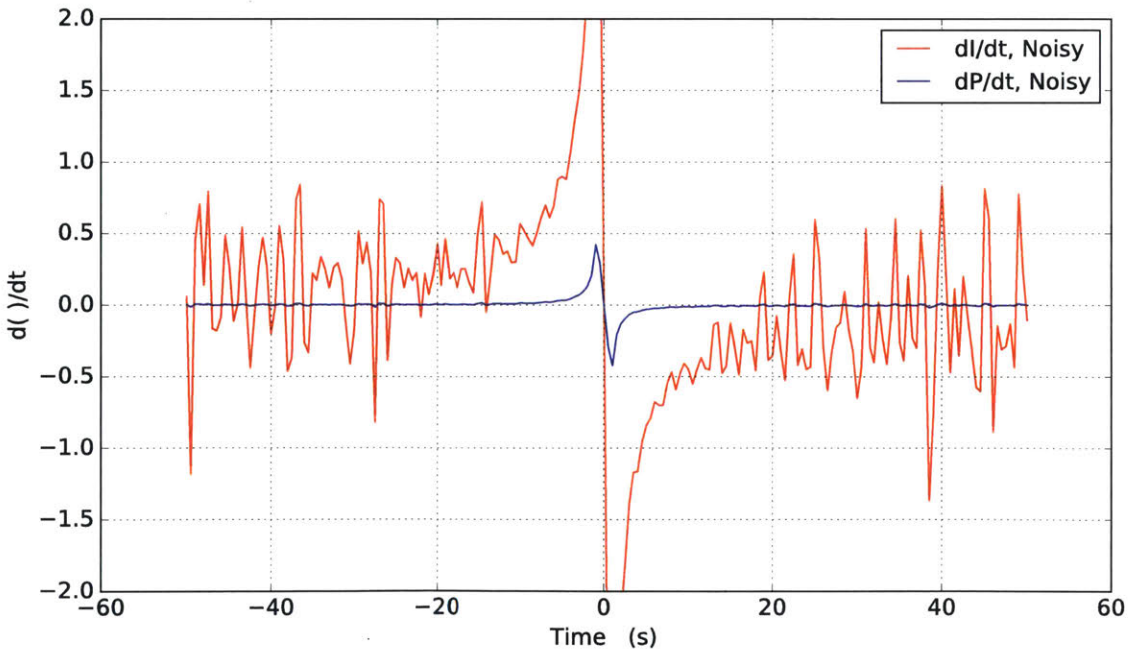

Figure 3-13: Gradient of intensity and pressure versus time, along a radial path of approach. Noisy signal simulated as Gaussian, with $\sigma = 0.001$.

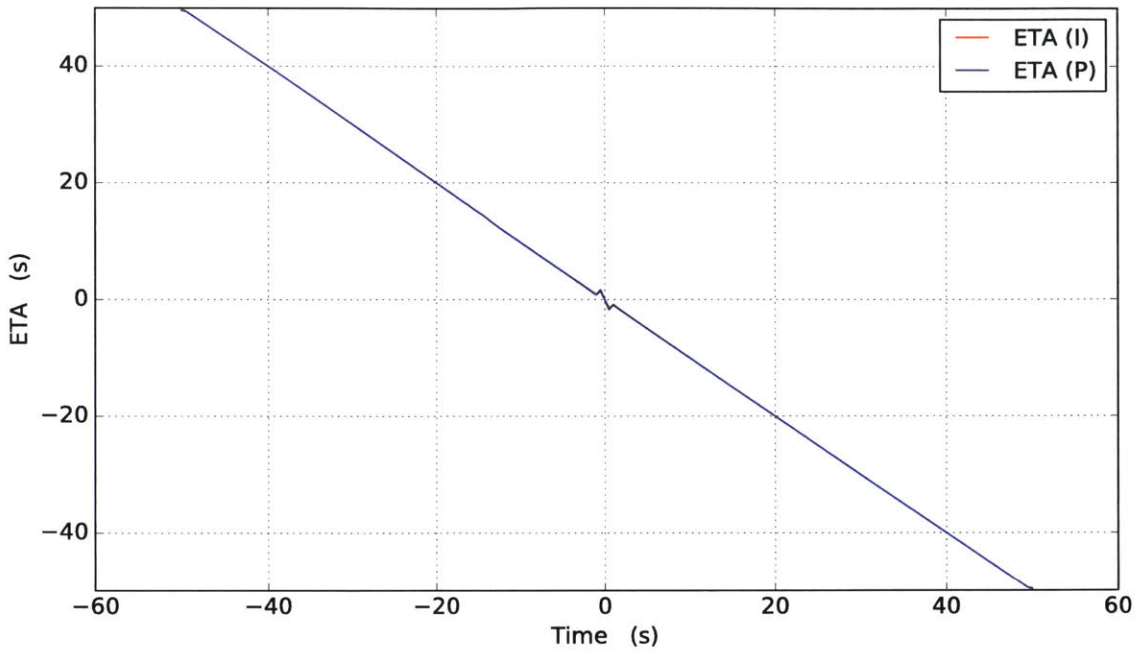

Figure 3-14: Estimated intercept time using intensity and pressure forms of ALPACA, along a radial path of approach.

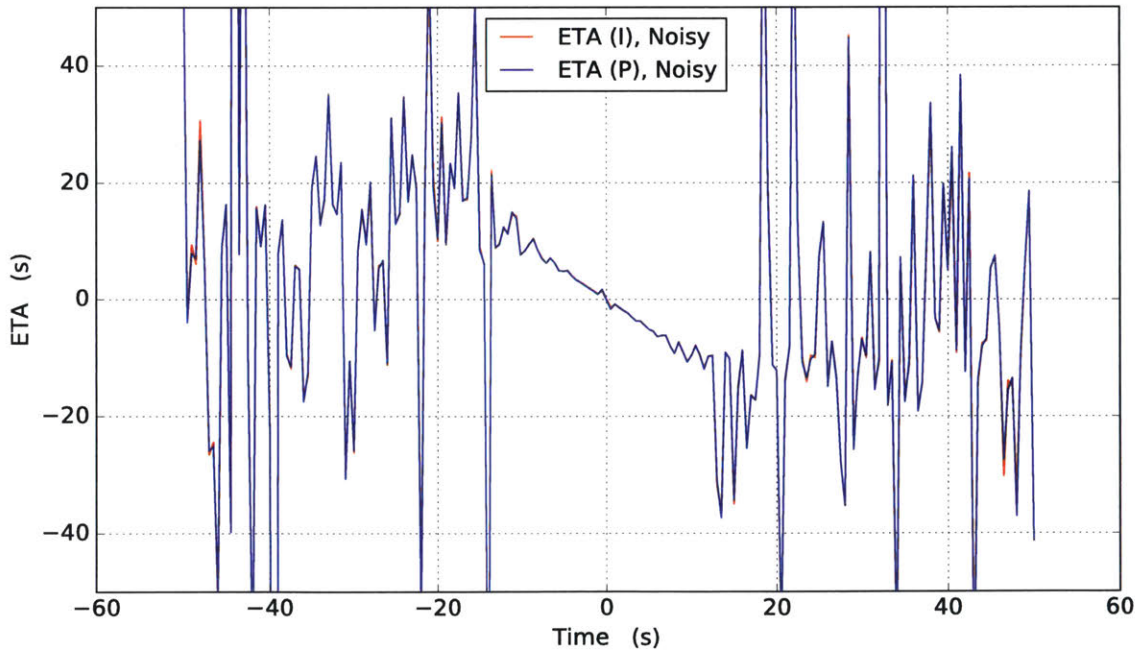

Figure 3-15: Estimated intercept time using intensity and pressure forms of ALPACA, along a radial path of approach. Noisy signal simulated as Gaussian, with $\sigma = 0.001$.

4 Experimental Configuration

The present chapter addresses the different sensor systems and experiments conducted during this work. Given the focus on shallow-water environments, and for the merit of easy access, experiments were conducted in the Charles River Basin. The MIT Marine Autonomy Bay, located at the Institute's Sailing Pavilion, served as the home of operations during vehicle deployments for this project. A prototype Bluefin SandShark was used as the AUV platform for autonomous deployments, while a standalone system based on the vehicle's payload was used for additional data acquisition with a different hydrophone array.

In order to facilitate the implementation of the system, some historical data available from prior work [13] was used for the initial software development. From there, an evolving series of deployments were used to collect additional datasets and to assess the performance of the system. Ultimately, a number of autonomous deployments were performed to test the system's ability to change behaviors in response to an approaching vessel.

4.1 Sensor Systems

4.1.1 Single Hydrophone Setup

The dataset used for initial development of the software modules necessary to run ALPACA online during autonomous missions was based on a single data channel, recorded in continuous mode at a rate of 44100Hz, using a dedicated desktop computer. These recordings formed part of prior work on this subject and were obtained from the preceding project's data archives, dating back to 2013. For that experiment, "the hydrophone was installed approximately 35m away from the dock, at a depth of approximately 2m in the water column" [13].

Data acquisition onboard the payload computer uses a triggered and windowed

recording frame, stored as separate files per trigger instance. For this reason, the legacy files had to be preprocessed in order to replicate the vehicle's data structure. The payload computer uses a GPS-synchronized pulse-per-second (PPS) signal to trigger the recording of a predefined number of samples per channel starting at the beginning of each second (see Sec. 4.1.2, 4.1.3 for more details). To match the payload data log format used in the earlier stages of this work, the audio files from 2013 were resampled to 37500Hz, and cropped to include only the first 8000 samples of each second[1]. The resulting files were then stored following the aforementioned data structure, and used as the basis for developing the software modules used in subsequent experiments.

4.1.2 Hydrophone Line Array

The hydrophone line array was built using a total of six elements mounted on an angle bracket, with ropes and weights used to adjust the array's depth and orientation from a boat or dock (Fig. 4-1). The hydrophones were connected via an analog high-pass filter circuit to a Measurement Computing Corporation USB-1608FS-Plus data acquisition system. The latter was then attached to a Raspberry Pi 3 single-board computer, used as a standalone testbed computer by running the same autonomy software employed onboard the SandShark payload.

Audio recording onboard the vehicle is triggered from a GPS-synchronized signal in order to provide a global reference frame in the time domain, for collaborative or localization systems based on time-of-flight. In order to enable use of such systems, and to replicate the AUV systems as closely as possible, the standalone system also used a globally synchronized PPS to trigger data acquisition. Because the computer enclosure for this system was built to remain above water, the PPS signal was obtained directly from the system's GPS module, for which a GARMIN GPS 18x LVC was used. Fig. 4-2 provides a data flow chart for this line array system. Further details on the development of this standalone testbed may be found in [12].

[1]Later code revisions have made these values configurable thru mission parameters.

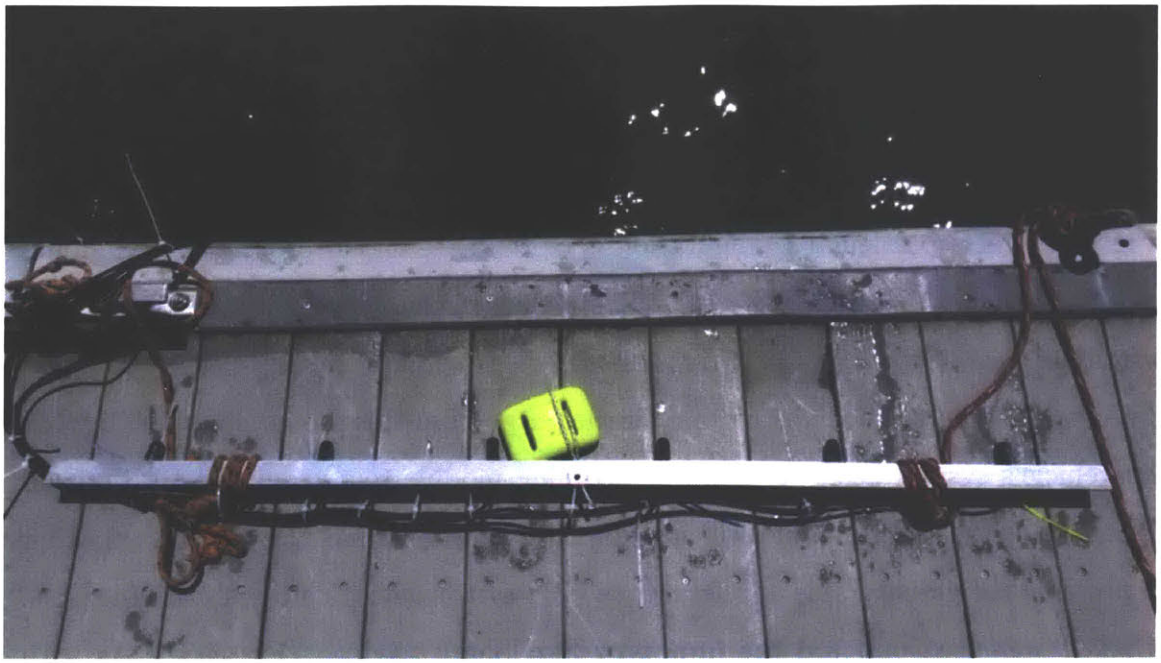

Figure 4-1: Line array with 6 channels and adjustable spacing.

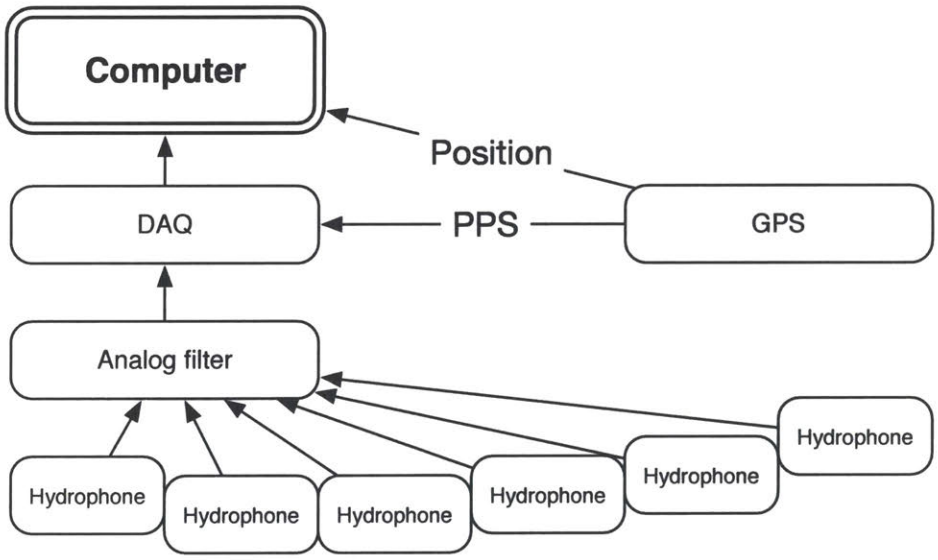

Figure 4-2: Data flow chart for line array with 6 channels and adjustable spacing.

4.1.3 Tetrahedral Array

A number of differences separate the AUV's hydrophone array from the line array used with the standalone test system. First and foremost among them, from a visual standpoint, is the array geometry, consisting of a 4-channel tetrahedral arrangement (Fig. 4-3). This particular configuration is of value for signal processing techniques such as beamforming (see Sec. 7.4). The element spacing used on the SandShark prototype also differs from the various distances tested with the adjustable line array. However, the most critical distinction for the purposes of this project may well be that the vehicle's system needs an additional timing module to provide the PPS trigger signal, since the GPS module will lose satellite contact while underwater. In order to preserve the global frame of reference, a GPS-synchronized chip-scale atomic clock (CSAC) was used onboard the prototype SandShark payload (Fig. 4-4). As with the line array testbed, additional information about the vehicle payload used for this experiment may be found in [12].

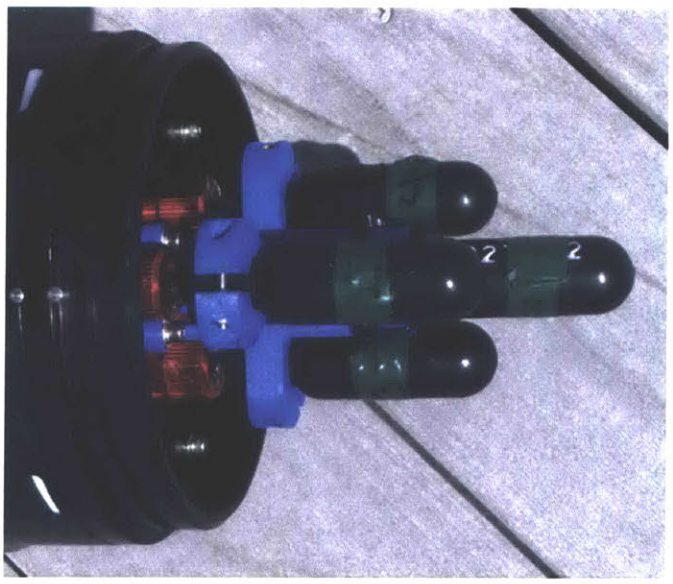

Figure 4-3: Tetrahedral array with 4 channels.

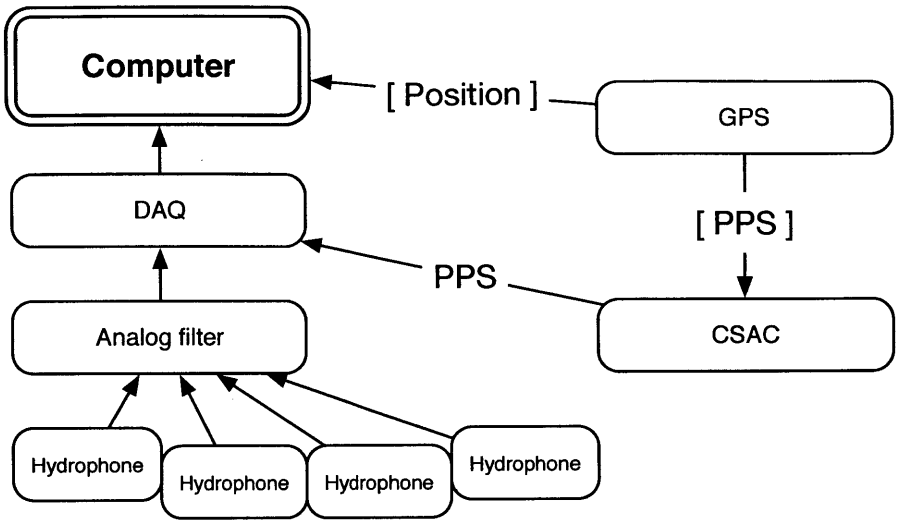

Figure 4-4: Data flow chart for tetrahedral array with 4 channels. Data from GPS module, shown in brackets, only available when vehicle is at the surface.

4.2 Experiments Conducted

In addition to using various sensor configurations, experiments were conducted in an escalating manner, to provide a measure of control over the increasing complexity of the system for data processing. This gradual stepping served to build upon the system by comparing the various measurements with the mathematical model and its physical meaning, as was detailed in Section 3. The various experiments conducted are detailed as follows.

4.2.1 Static-Receiver Collection

The static-receiver experiments were used as a basis for software development and data processing, and consisted of anchoring the sensor system in a fixed location for the duration of the experiment. This category includes the measurements taken from prior work (from the 2013 experiments), as well as the data collected with the line array system.

Holding the sensor array in place served two purposes. First, it provided a reliable basis for relative range computation when GPS data from the vessel used as a noise source was available, as the receiver location was known and non-changing. Second,

it provided a dataset with reduced noise, in the absence of the array carrier vessel.

The two features drawn from a static receiver facilitated progress of the software modules, to ensure proper processing of the acoustic signals onboard the AUV. Additionally, they provided supplementary datasets during AUV deployment missions.

4.2.2 Moving-Receiver Collection

Moving-receiver data acquisition was conducted with the AUV-mounted tetrahedral array during missions not yet responsive to approaching threats. Basic missions such as racetracks and loiters, as well as more advanced autonomous missions defined in the repositories of the Laboratory for Autonomous Marine Sensing Systems, were used as the basis for vehicle behavior during these tests.

The collection of data using the AUV, in the absence of behavior triggering, was used to develop a better understanding of the effect the vehicle's own noise, added to its displacement, may have on the measurements. These results were considered when defining the thresholds selected for the subsequent behavior-triggering experiments.

4.2.3 Behavior-Triggering Experiments

The behavior-triggering experiments sit at the heart of this work. Ultimately, the purpose of implementing the ALPACA intercept-time estimator is to enable collision avoidance responses based on the system's detections. As such, this last set of tests mark the project's turning point, where an AUV's active behavior is directly affected in response to an approaching threat throughout the duration of an autonomous mission.

To select and assemble the test scenarios, the following idea was first considered: autonomous missions cover a wide range of objectives, and the vehicle's decision capabilities are generally built to fit the various probable scenarios foreseen by the operator. In the purview of this work, even simple path-based objectives serve as suitable examples of AUV deployment in shallow water. A lawnmower path could be used to collect measurements, or perform imaging or scanning, over a given area. A

racetrack may be chosen for extended monitoring, or a loiter path may be used as a station-keeping behavior. These path-based behaviors define sensible and realistic use scenarios, while their simplicity make them easier to implement, and thus they served as the building blocks for the experiments herein detailed.

Two of the path behaviors previously mentioned were selected, such that one would serve as the vehicle's main mission and the other would correspond to the collision avoidance mode. The secondary behavior was triggered by the ALPACA module through an alarm control variable on the `MOOSDB`. For this basic test scenario, a timer feature was used in order to reset the alarm flag after the countdown ended. Once the state of alarm was reverted, the vehicle was allowed to resume its original behavior until another intercept event occurred, or the AUV's mission was completed.

Prior to vehicle deployment, the various behaviors and mission processes were tested within a computer simulation environment, to verify that all software modules were operating as intended. For these virtual experiments, the data collected from earlier measurements with both receiver geometries (tetrahedral and line array) were used as input for the simulated acoustic sensor. Figs. 4-5 and 4-6 show the vehicle responding to the acoustic data input. Once sufficient simulation testing had been completed, the software was transferred to the vehicle computer for in-water testing.

The final tests were performed with the Bluefin SandShark AUV in the Charles River Basin. Motorboats from the MIT Sailing Pavilion were used as noise sources during operations. Additional acoustic sources tested included a jet-drive kayak, as well as an underwater speaker configured to emit a frequency-ramping chirp every second. Tests with the motorized vessels were conducted such that different ship speeds and closest ranges of approach were recorded. Numerous passes were performed for each case. When available, the surface ship's position was recorded with a GPS logging system. The speaker-based tests were conducted while holding the acoustic source in place, and observing the effect that the AUV's own displacement would have on the intercept module; this was done in giving consideration to scenarios where known noise sources may be present as part of an acoustic navigation system (see 7.4).

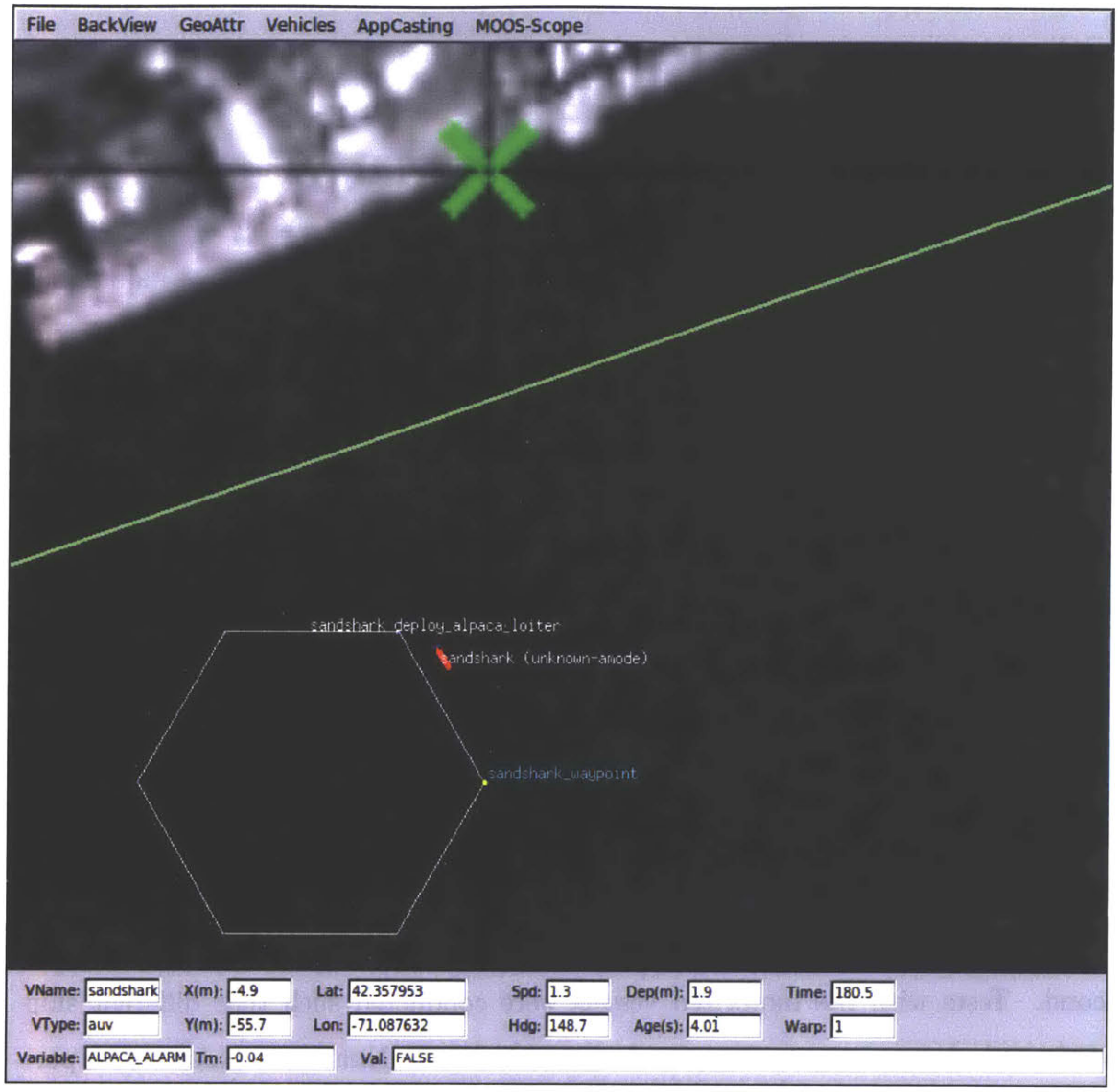

Figure 4-5: Simulation of SandShark deployment, with the main mission set to tracing a loiter path. `ALPACA_ALARM` set to `FALSE`.

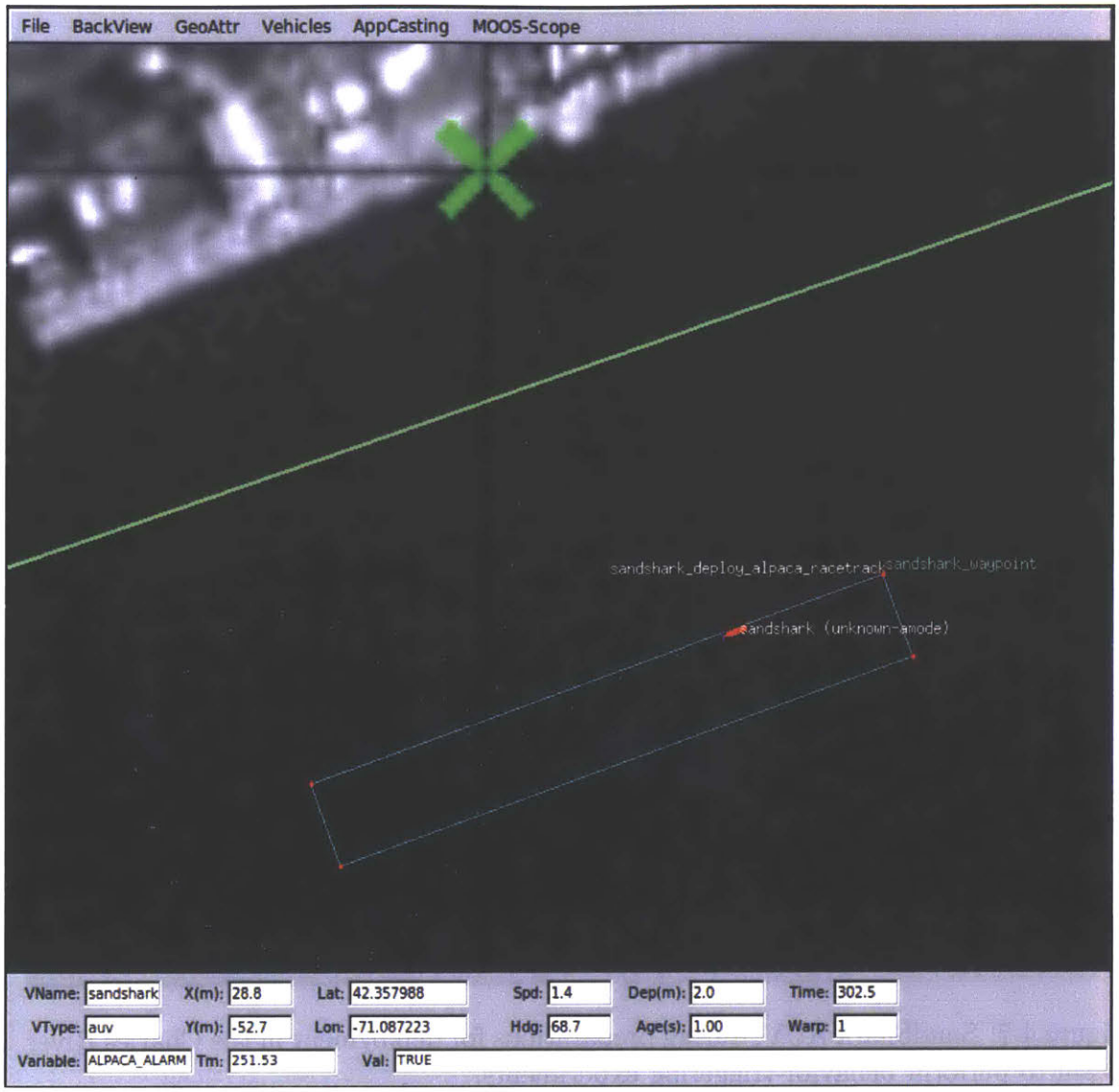

Figure 4-6: Simulation of SandShark deployment, with the alarm-triggered behavior set to following a racetrack path that extends outside of the loiter field. `ALPACA_ALARM` set to `TRUE`.

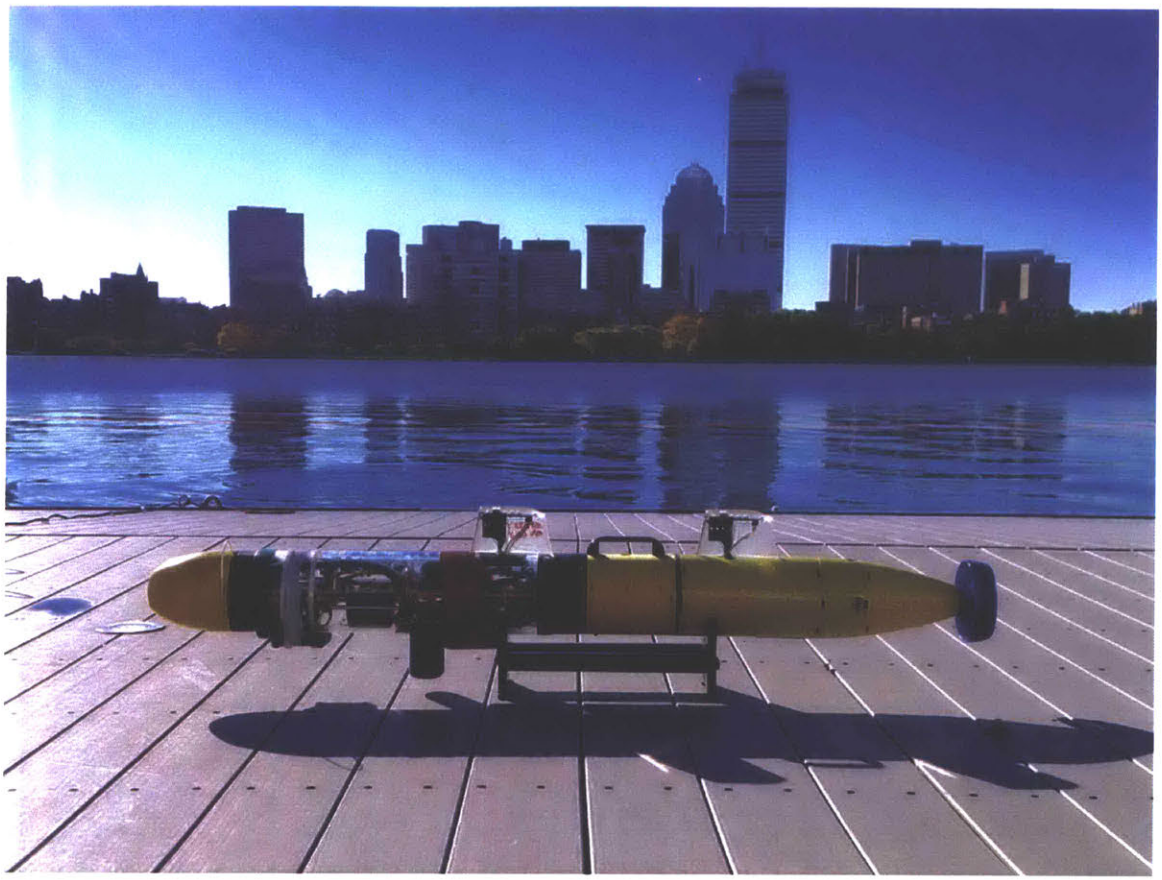

Figure 4-7: SandShark AUV, during preparations for deployment in the Charles River Basin to perform behavior-triggering experiments.

5 Results and Discussion

When testing a sensor system, many variables come into play. Some of these changes can be well accounted for within the base model, while others deviate significantly from the original assumptions. For a system intended to further facilitate autonomous operation of an underwater vehicle during deployment, as is the case with this project, understanding how real measurements may deviate from the base scenario can lead to significant improvements in the system's responsiveness and reliability. In order to better illustrate the increments in complexity of the system, and the development progression used through this work, the results are presented in direct comparison to the model described in Section 3 through a series of case studies. Thereafter follows a discussion of the challenges seen in online signal processing during AUV deployment.

5.1 Post-Processing of Static-Array Acoustic Logs

Prior to implementing an online version of the ALPACA system on an AUV, data obtained from the preceding 2013 experiment's archive and acoustic logs collected with the different arrays described in Section 4 were used to develop the software modules needed. This section presents a sample case-study performed during post-processing to evaluate the performance of the system. This type of analysis began with a visual inspection of the acoustic data in the form of root mean square (RMS) of the voltage per second. Fig. 5-1 shows the data collected with the dock-mounted line array during a 20-minute span.

Under the scenario discussed earlier, of a motorboat moving along a travel lane at near-constant speed, each slow-rising peak reflects a gradual increase in acoustic power that could be associated with an approaching vessel. The narrow spikes may be associated with a wide range of transient events, of acoustic or electronic nature alike, but are too brief to correspond with a nearing ship. Fig. 5-2 shows the event occurring around $t = 434$s in the previous dataset. The event peak is marked by the

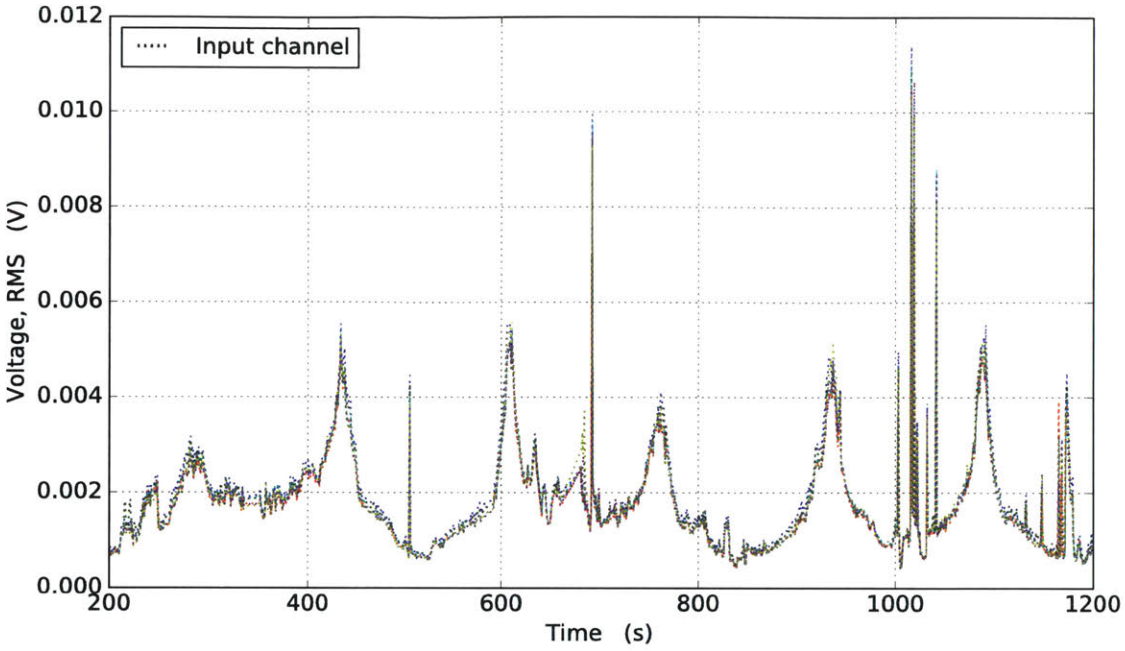

Figure 5-1: RMS of hydrophone voltage measurements collected in the Charles River Basin with a 6-ch line array, during a 20-min span on Aug. 2, 2016.

red vertical line. Looking closely at the signal from the various channels, it may be observed that there is a small difference in gain for each input, but they otherwise exhibit similar features for the RMS voltage. The average of all channels for each measurement cycle in time is given by $\overline{V}$.

Hydrophones provide a roughly proportional correlation between sensed pressure P and the output voltage V, with some edge effects related to saturation. Where valid, this ratio $P/V = \alpha$ will carry over through the RMS and gradient computations. Thus, under the assumption that the sensor's boundary effects may be dismissed, the pressure form of the ALPACA system and its intercept-time estimation (Eq. 3.9) may be expressed in terms of the voltage measurements directly. Following the same approach as was presented in Section 3, Fig. 5-3 shows the gradient of the RMS voltage for the event presented above. As addressed in Section 3.4, noise in the input signal can introduce significant variation to the intercept time estimation and may render the results ineffective. Such results are presented in Fig. 5-4.

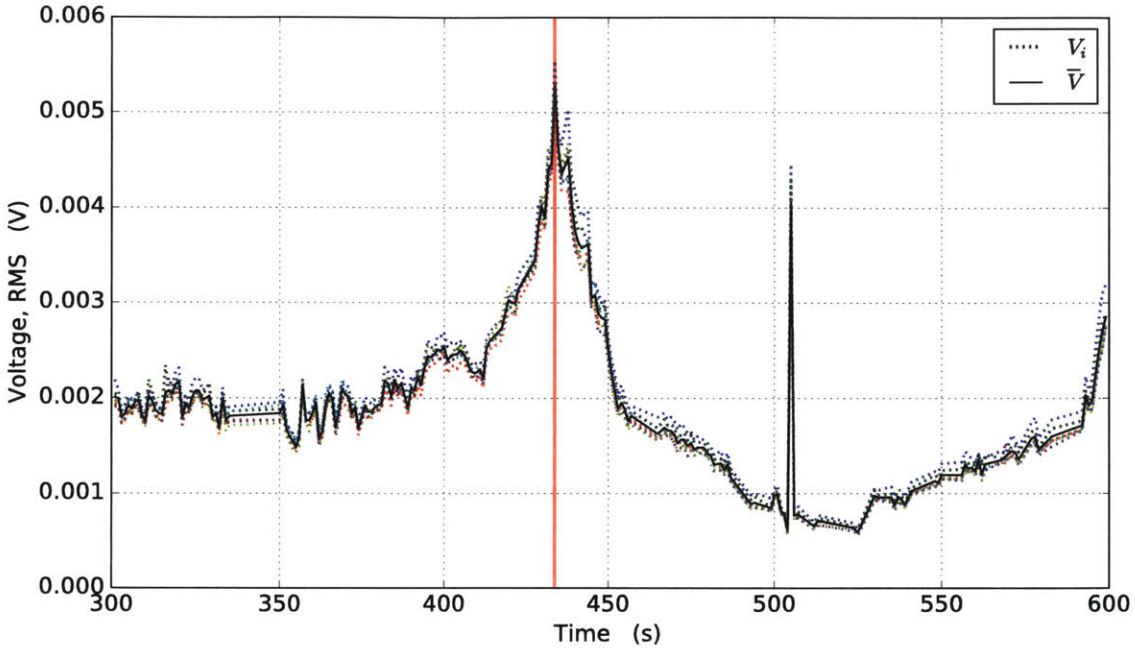

Figure 5-2: RMS of hydrophone voltage measurements collected in the Charles River Basin with a 6-ch line array. Single event case study.

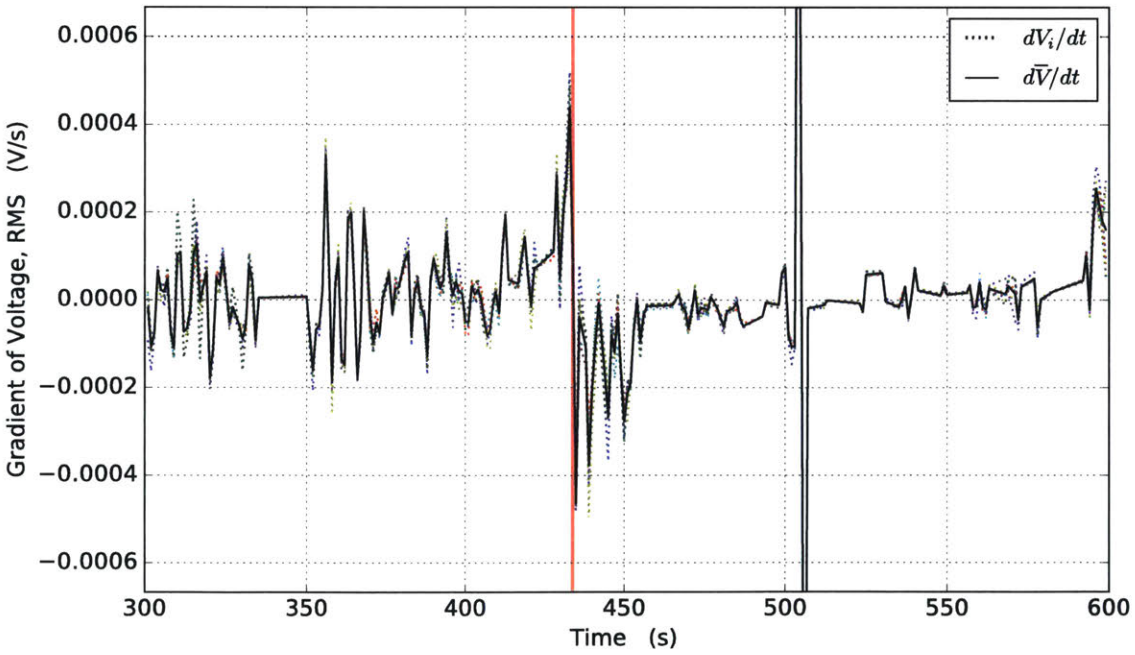

Figure 5-3: Gradient of RMS voltage measurements collected in the Charles River Basin with a 6-ch line array.

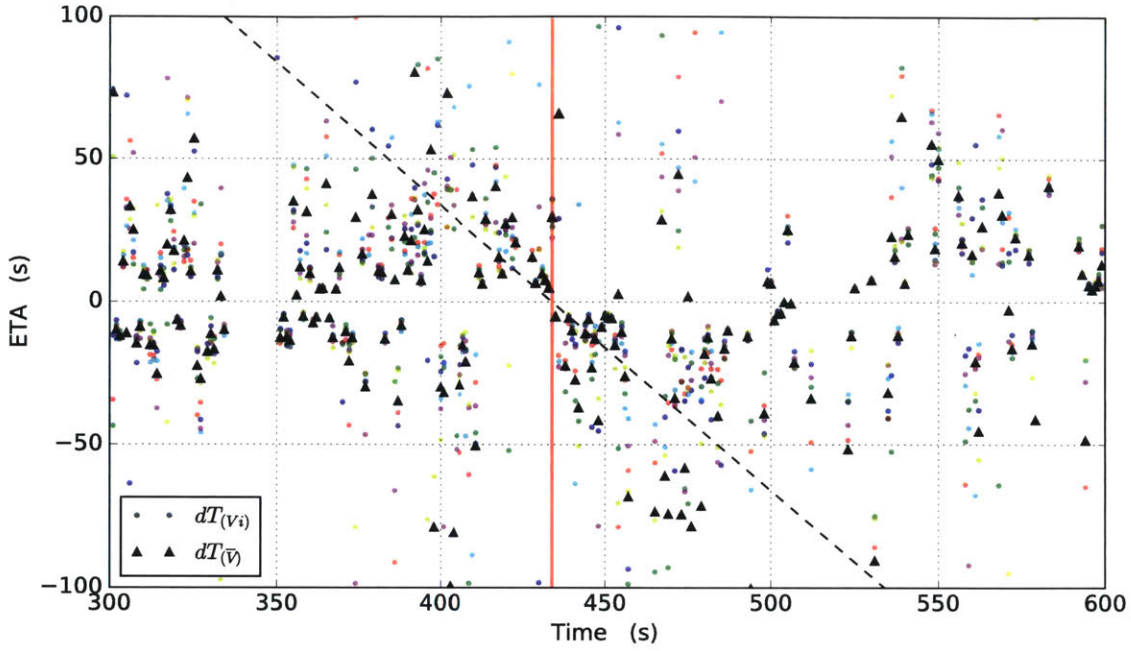

Figure 5-4: Intercept time estimates based on point-to-point gradient of RMS voltage.

5.1.1 Signal Processing

Given that the ALPACA estimator is highly sensitive to noise, appropriate signal processing is fundamental to achieve results upon which the AUV may base behavioral decisions. Various methods exist to perform signal smoothing, or to account for outliers in a set of measurements. This section discusses the various approaches evaluated during this work.

Desirable for its simplicity, a running average method can smooth out the fluctuations in the signal and provide a sense of the slow-evolving trends sought in this intercept alert system. However, this approach presents two notable limitations. First, the size of the observation window introduces either a delay or lag in the signal, depending on how the local average is aligned with the observation window's time range. The second limitation is that it may be affected by extreme outliers. Figs. 5-5 and 5-6 show the 10-point running average of $\overline{V}$. In the 500-550s time frame, the effects of the single extreme outlier can be observed for both the amplitude and gradient values.

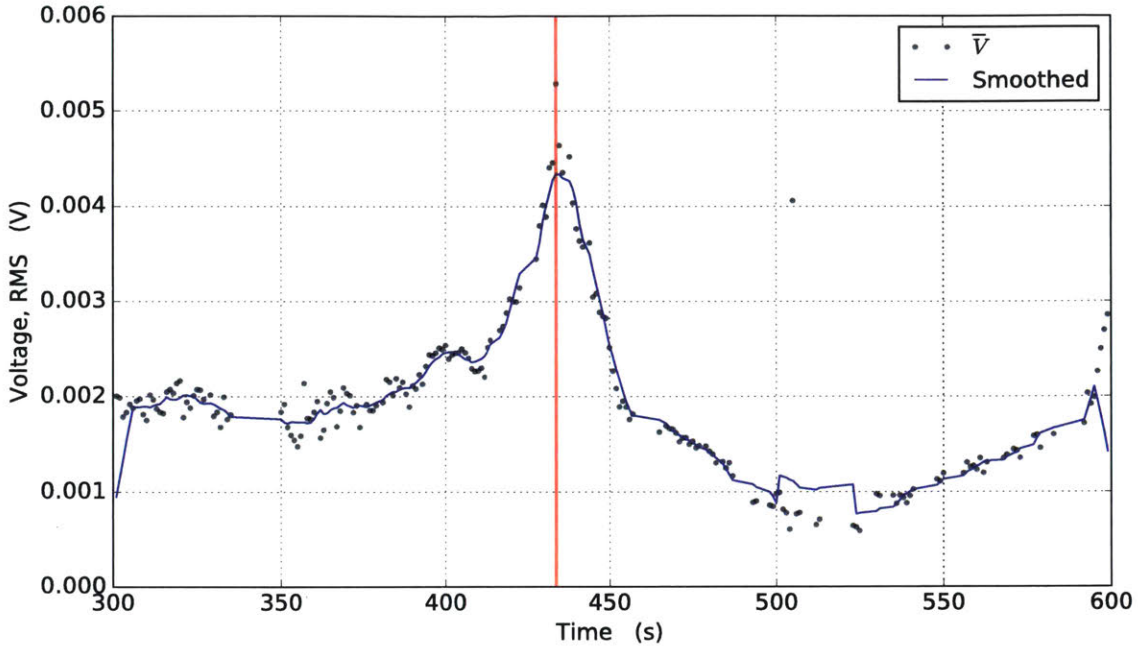

Figure 5-5: RMS of hydrophone voltage measurements, using a 10-point running-average smoothing window.

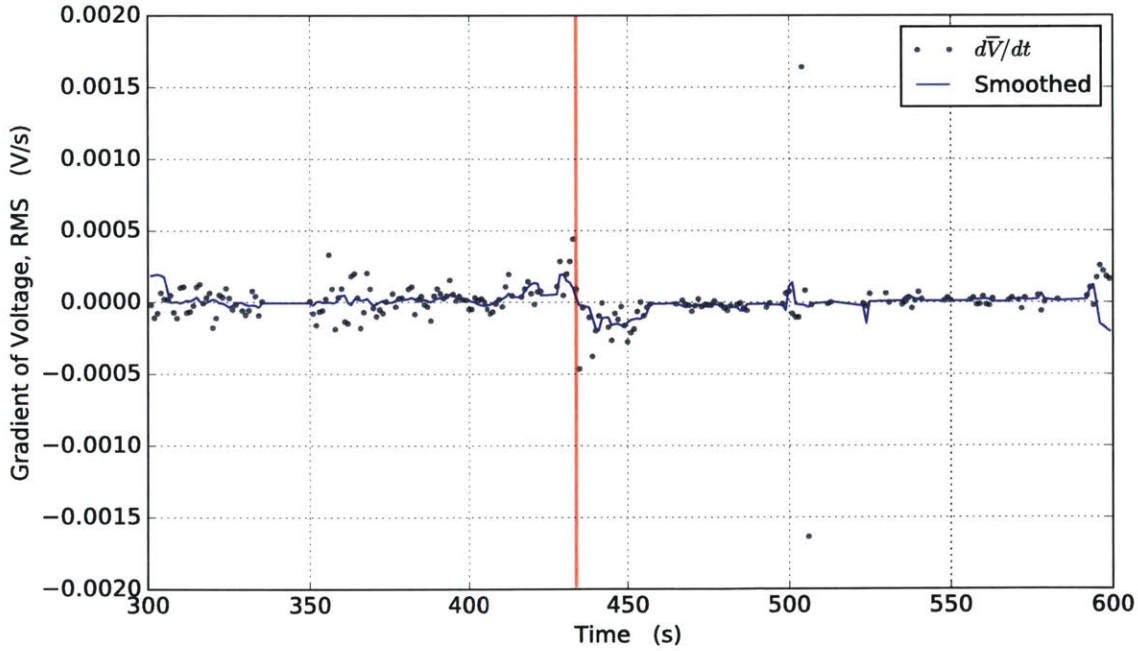

Figure 5-6: Gradient of RMS voltage measurements, using a 10-point running-average smoothing window.

Despite its limitations, the running average method carries notable advantages against the unsmoothed output. Fig. 5-7 isolates the $\overline{V}$ values from Fig. 5-4, while Fig. 5-8 shows the intercept time estimated from the smoothed signal. While it may be difficult to discern a trend in the former, the latter exhibits a more apparent cluster around the reference line of unit slope near the intercept point. Comparing the latter figure with Fig. 3-9, it may be noted that the convergence behavior observed approximates the model's expectation.

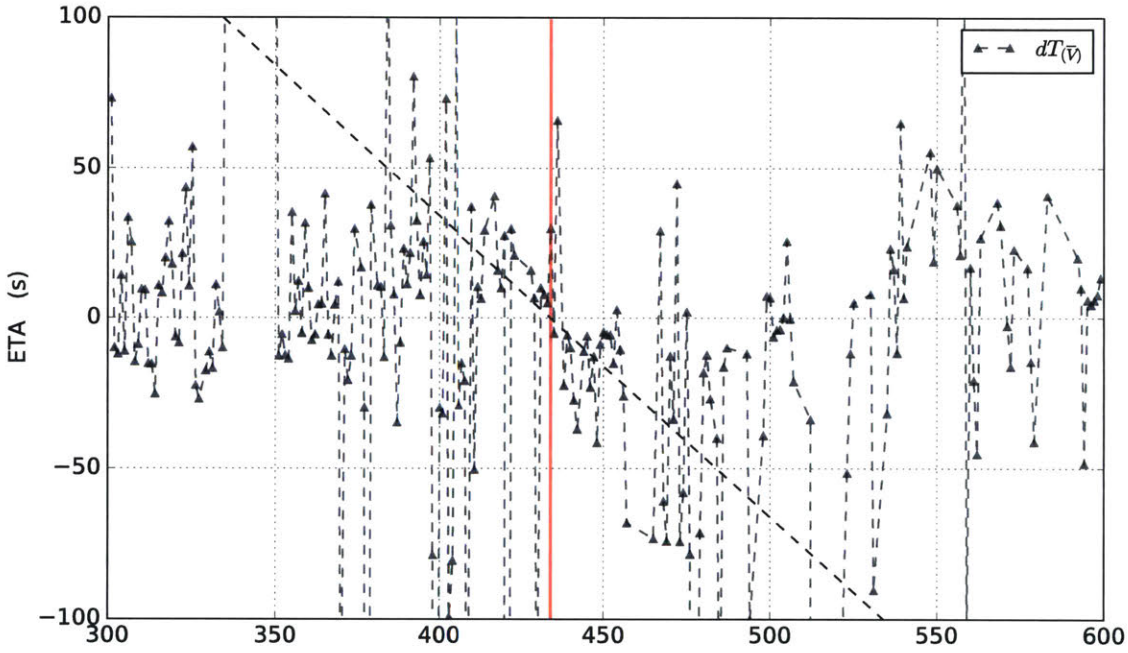

Figure 5-7: Intercept time estimates based on point-to-point gradient of RMS voltage.

Regarding the use of an observation window, as may be the case for the AUV with its data buffer, it is worth noting that the length of the span used will have a significant effect on the system's output. Drawing from the limitations described earlier for the running average, it was noted that the effect of an extreme outlier certainly carries over in the amplitude and derivative values. The spreading effect that the running average has on the data introduces an argument for compromise between the system's sensitivity and responsiveness. In other words, a larger window will do a better job of softening out the outliers, but will also make the system slow to respond. Because the acoustic profile expected by the mathematical model is non-

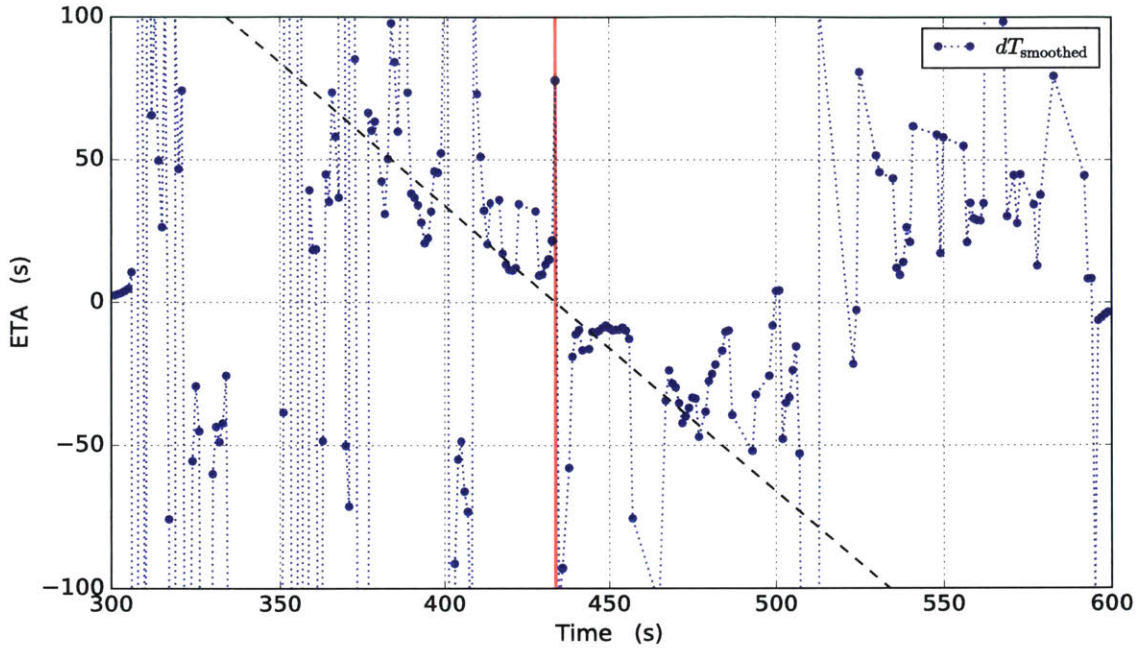

Figure 5-8: Intercept time estimates based on smoothed gradient of RMS voltage, using a 10-point running-average of the measurements.

linear, the slow response of the windowed average might also render the estimator ineffective as the incoming vessel draws near.

The manner in which a slow response may harm the system's performance might not be readily apparent. Fig. 5-9 shows how a wider observation might suggest a suitable prediction in a more timely fashion. However, the data represented in the figure is centered on the observation window as it travels along the dataset. Consequently, the vehicle would have to account for the half window length of time that separates the prediction from then-current time. Furthermore, the figure shows how the windowed average causes the predicted intercept time to diverge near the singularity. This stems from the cropping effect the smoothed values have on the real acoustic peak (Fig. 5-10). This phenomenon causes the smoothed data to more closely approximate the case of a further offset travel lane, as was presented in Fig. 3-2. The divergence around the critical point also reflects the corresponding shift induced by the averaging method. Furthermore, because of the window width, the vehicle would only have access to the estimates shown, after a delay of half the window length.

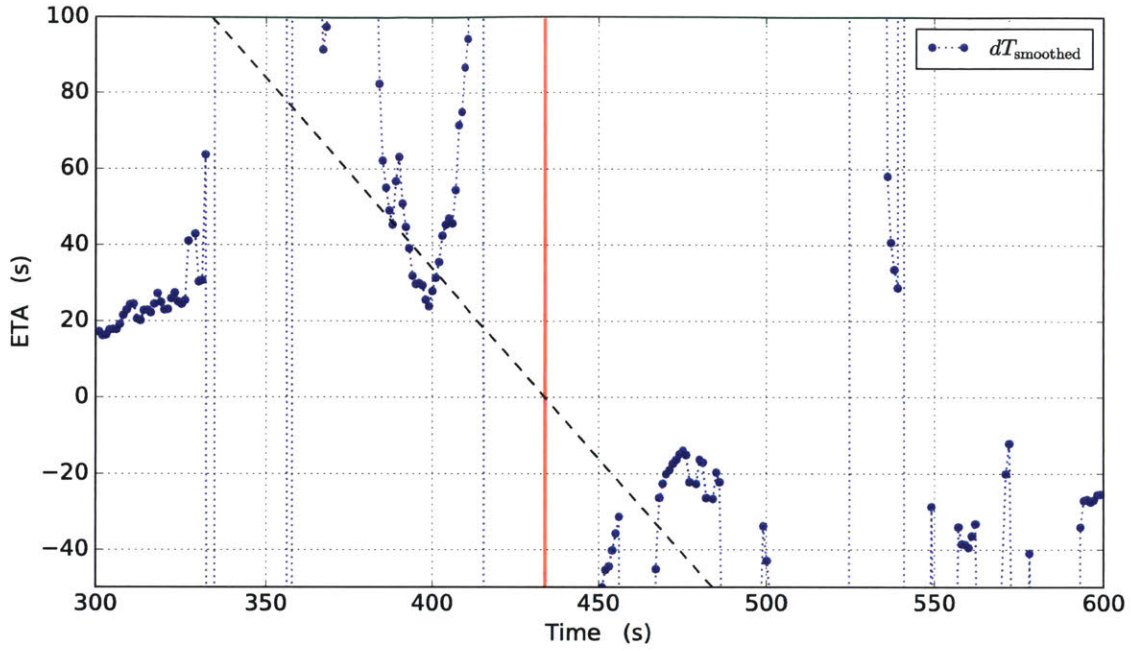

Figure 5-9: Intercept time estimates based on smoothed gradient of RMS voltage, using a 60-point running-average of the measurements. Average values centered on observation window; intercept estimate reported to vehicle would have a 30s delay.

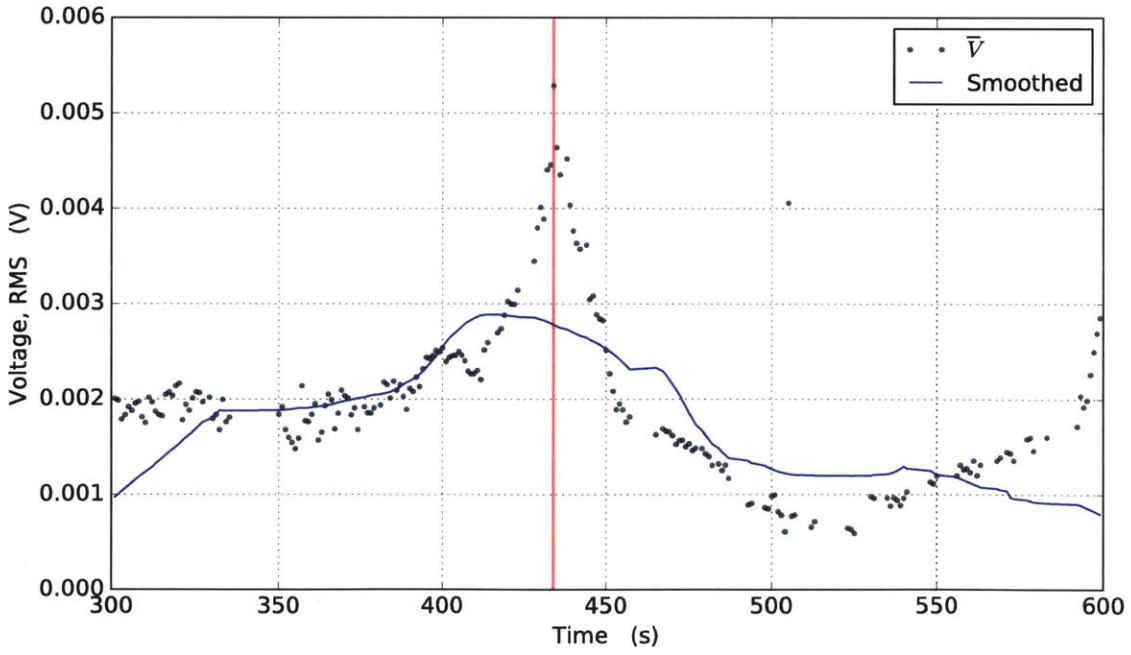

Figure 5-10: Intercept time estimates based on smoothed gradient of RMS voltage, using a 60-point running-average of the measurements. Average values centered on observation window.

5.1.2 Model-Based Curve Fitting

The expected profile, as given by the mathematical model, is characterized for its single peak at the point of closest approach. In order to compare the performance of a running average method with an alternate curve-fitting approach, a Lorentzian function was used as the base model. Given by its peak amplitude A, its full-width at half-max Γ, its center t_o and a constant offset C, the Lorentzian function can be expressed as Eq. 5.1.

$$L(t) = A \frac{(\frac{1}{2}\Gamma)^2}{(t - t_o)^2 + (\frac{1}{2}\Gamma)^2} + C \tag{5.1}$$

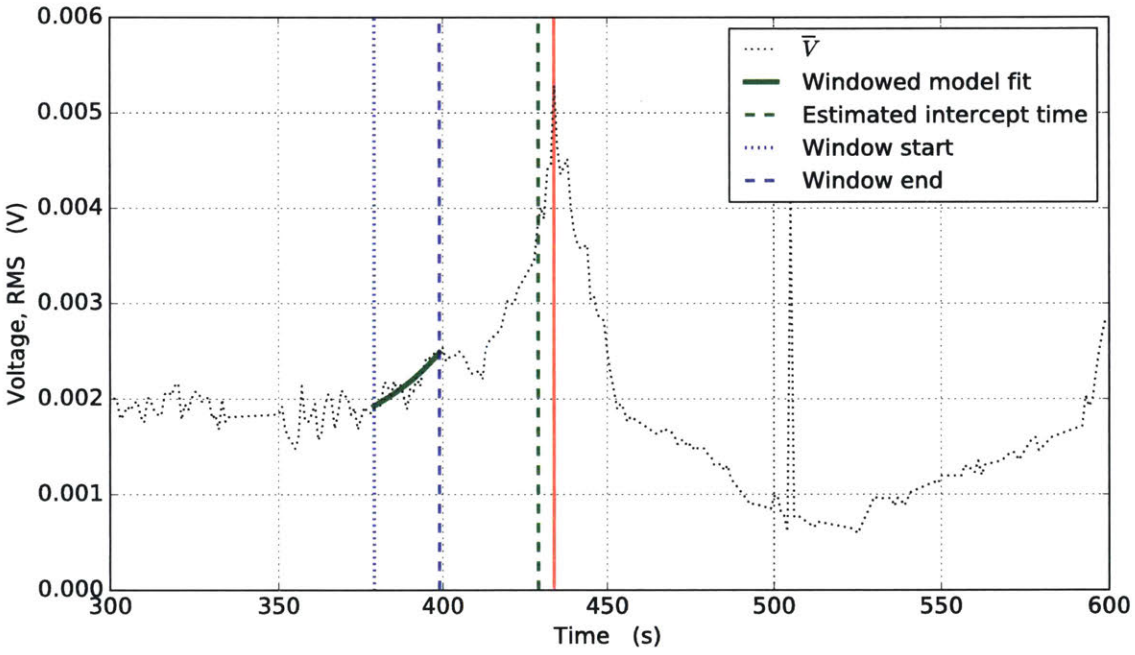

Figure 5-11: Overlay of an observation window fed to a curve-fitting routine, and the extended time-series of RMS voltage measurements. Actual peak (red) and estimated intercept time (green) shown.

Using an observation window method, as with the running average, the visible measurements where fed to a curve-fitting routine based on the Lorentzian function above. The parameters found by the optimization routine were then used to compute the corresponding voltage amplitude at the then-current time. Designating the leading edge of the window as $t = 0$ for each step, the peak center t_o was then di-

rectly related to the estimated time to arrival dT. Fig. 5-11 shows the overlay of a 20-point observation window over the dataset, the model fitted to the data set, and the projected intercept time. The series of leading-edge values were then plotted as in Fig. 5-12, for visual inspection of the curve-fitting performance. Intercept times obtained from the curve-fitting routine are shown in Fig. 5-13 for the average measurement series $\overline{V}$, and in Fig. 5-14 for all channels individually.

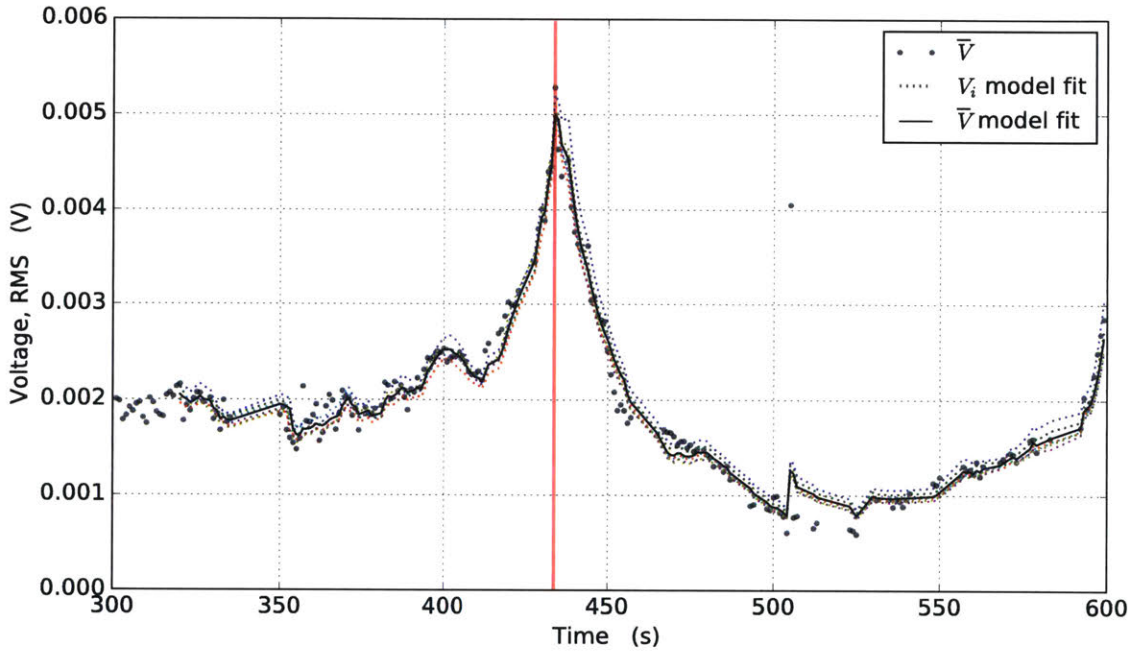

Figure 5-12: RMS voltage based on curve-fitting model with a 20-point observation window. Fit per channel and fit to average measurement $\overline{V}$ shown.

Comparing the model fitting output with the preceding results, a few notable differences appear. Unlike the running average method, the curve-fitting routine does not readily introduce a measurement delay due to the window size. Instead, parameters are provided based on the leading edge of the observation window, corresponding to the true then-current time from the vehicle's perspective. On the other hand, because the Lorentzian function describes a single peak, the estimator may tend to track a trailing peak, identifying it as the latest event of interest until enough additional information shifts the windowed data towards a new maximum (see Sec. 5.2 for more on local peaks). This can be identified by the drop in amplitude shown on

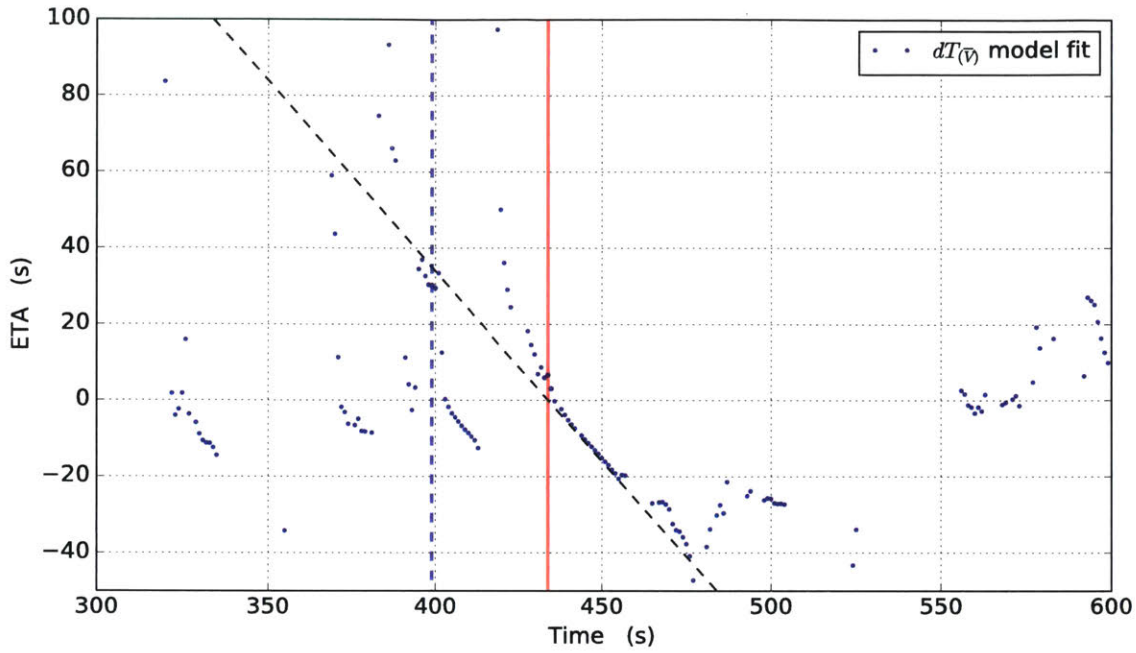

Figure 5-13: Intercept time estimates based on model fit of average RMS voltage $\overline{V}$, using a 20-point observation window.

the right-hand side of the leading edge in Fig. 5-11, marking a local peak.

The shift to negative values of dT, as shown in Fig. 5-13 and Fig. 5-14, indicate that the curve-fitting routine is converging on a solution centered on the local peak. This shift can be observed to the right of the leading edge in the intercept time plots. It may be remarked, however, that a noteworthy cluster of reliable and actionable measurements are available to the vehicle by this point, as seen left of the leading edge in the aforementioned figures. Furthermore, a double-cycle approach may be used to determine whether the threat has passed, by checking the predictions preceding the latest peak. Should the predictions align with the local maximum, it may be determined that the threat of collision has passed. However, should the predictions computed prior to the local peak point to a time in the future, the vehicle could assume that the threat might still be underway. Tracking the latest event of interest, then, tells the system what predictions it should act upon for decision-making, until enough additional measurements have been collected or enough time has passed.

In order to account for the presence of small local peaks, tests were performed

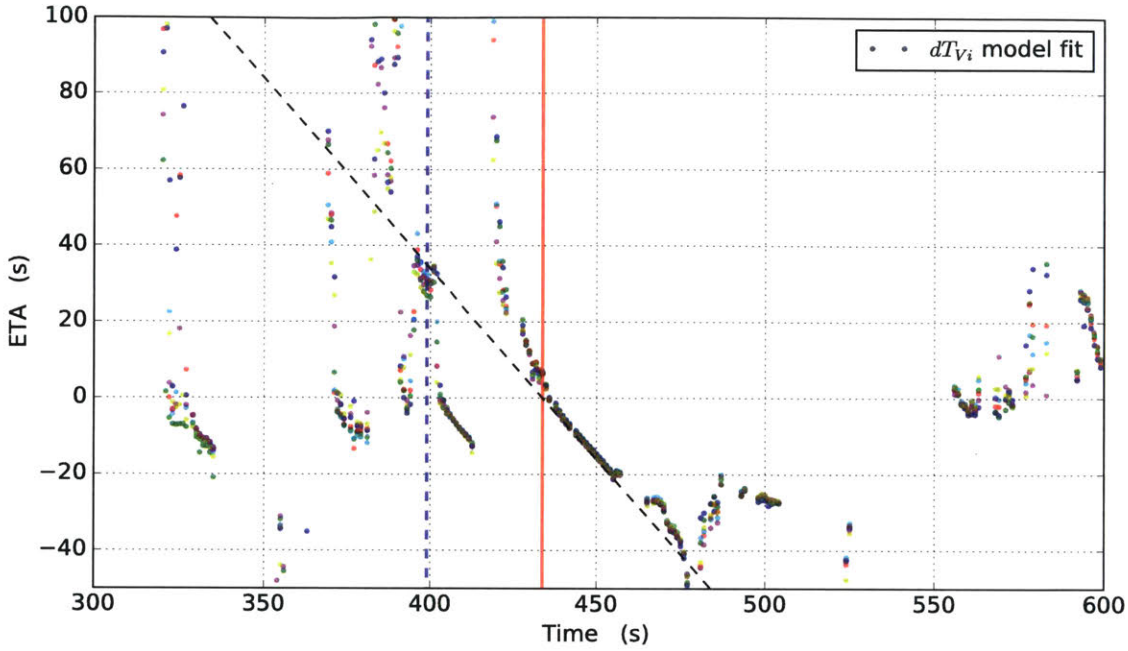

Figure 5-14: Intercept time estimates based on model fit of V_i, the RMS voltage per channel.

by changing the span of the observation window. However, as discussed earlier, this parameter may introduce various unwanted effects. Instead, a variation of the model was also tested. Working on the assumption that any approaching vessel would necessarily pass dangerously close to the receiver, the model was conditioned to exclusively reflect radial approaches. By forcing the model directly over the singularity, the estimator would struggle to converge on the departure segment of a passing vehicle, but would likewise be less sensitive to smaller local peaks on the approach leg. The results obtained with the radial model are shown in Fig. 5-15.

5.2 Variable Travel Lanes

The mathematical model used for this work starts from the assumption that a given boat is operating at a constant speed, such that its acoustic source level may be assumed constant. Further, the base scenario described was that of a vessel traveling on a straight path. Even when the AUV may be moving, so long as it too follows a

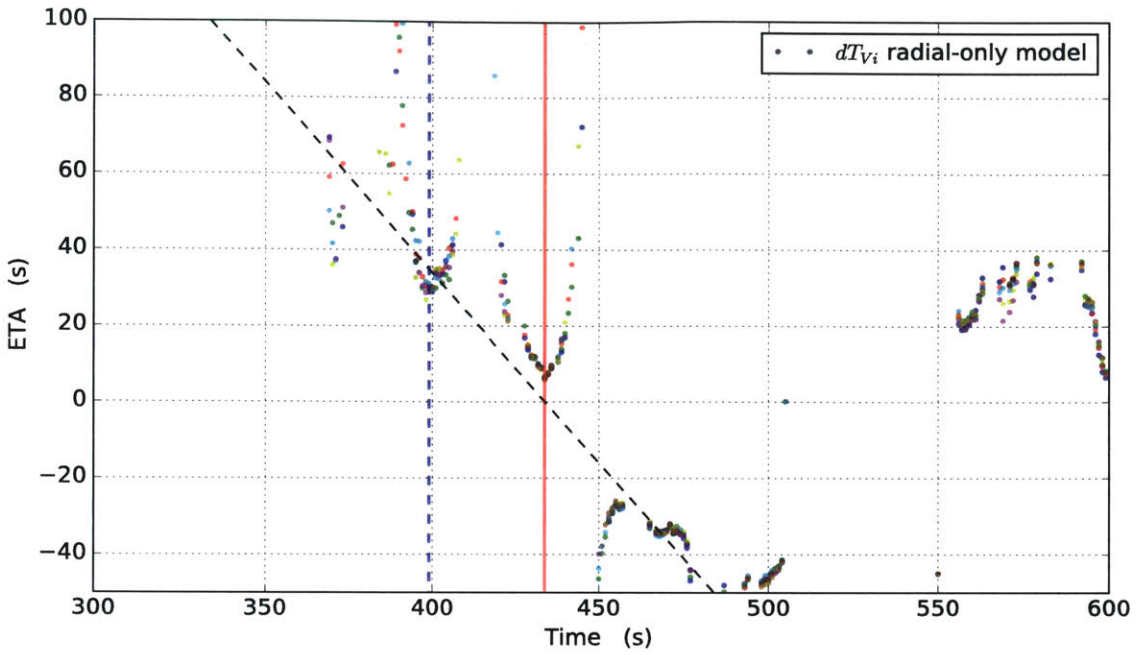

Figure 5-15: Intercept time estimates based on radial-only model fit of V_i, the RMS voltage per channel.

linear path, the relative velocity vectors remain unchanged. However, expecting both ship and AUV to follow such a pattern at all times is both unreasonable and unlikely. There will be times when either vessel will change course or adjust their speed while in range of this acoustic detection system, which will ultimately alter the results.

An interesting scenario to consider would be that of a ship gradually changing course, as if following a curved path or even driving in circles. By changing course and therefore varying the relative velocity vector between the two vessels, the ship would necessarily alter its time of closest approach, or intercept time. Similarly, discrete changes in speed may alter the motor noise power, as well as the relative vector. This type of pattern was encountered during the various tests, and one such case taken from the 20-minute is presented in Figs. 5-16 through 5-19.

It must be noted here that while the occurrence of a variable path profile in the case study shown above is consistent with both the theory and the notes taken during the experiment, the exact ship path and speed could not be determined from the data logs due to loss of signal on the motorboat's tracking device during this stage of the

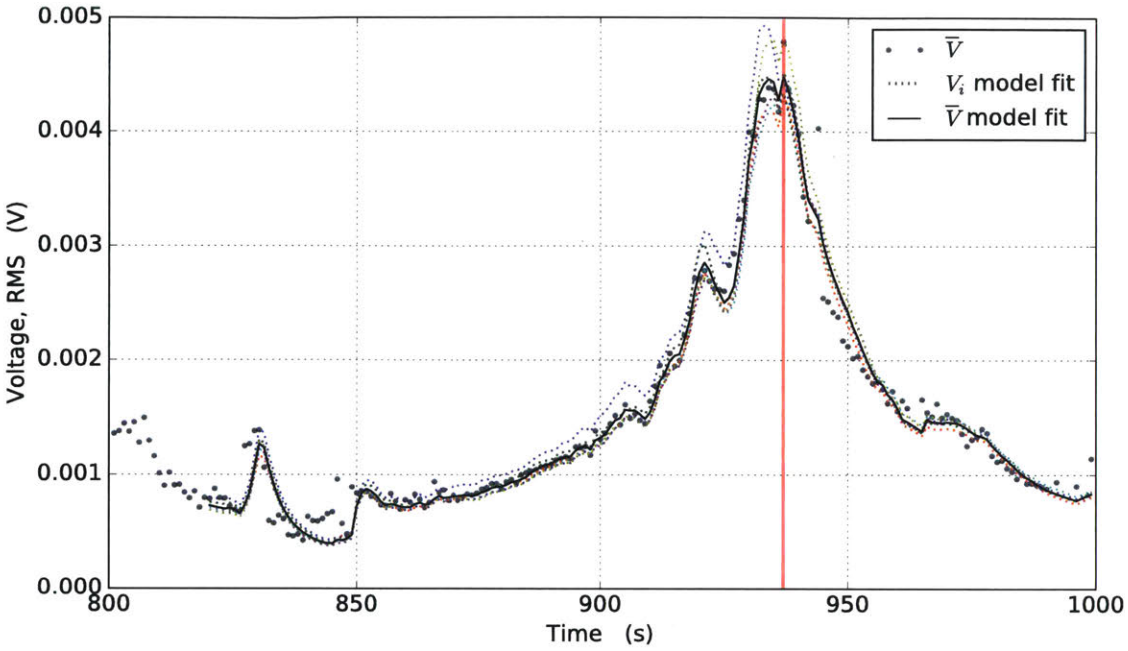

Figure 5-16: RMS voltage based on curve-fitting model with a 20-point observation window. Fit per channel and fit to average measurement $\overline{V}$ shown. Variable path case study.

experiment. However, the figures above exhibit a number of features worth discussing in the scope of this work, even in the absence of GPS tracking data.

Following the sequence used in earlier sections, the first step was to perform a visual inspection of the voltage amplitudes. In Fig. 5-16, three distinct peaks may be observed in the 900-950s timeframe. In the subsequent figures, the various intercept estimation methods reflect a similar clustering trend: the estimates tend to converge around a unit slope line prior to each peak, and then shift forward after passing the local maximum. This shift of the prediction groups suggest that a defining parameter in the environment is changed. A number of possibilities exist to induce this type of behavior, of which the following are two possibilities described to illustrate the complexity of the system. A single change in the motorboat's course would not cause the amplitude to drop unless the vehicle steered away from the receiver, but an evasion maneuver could point the ship away from the receiver for a brief moment and then back on approach as it resumed course. A change in speed could drop the source

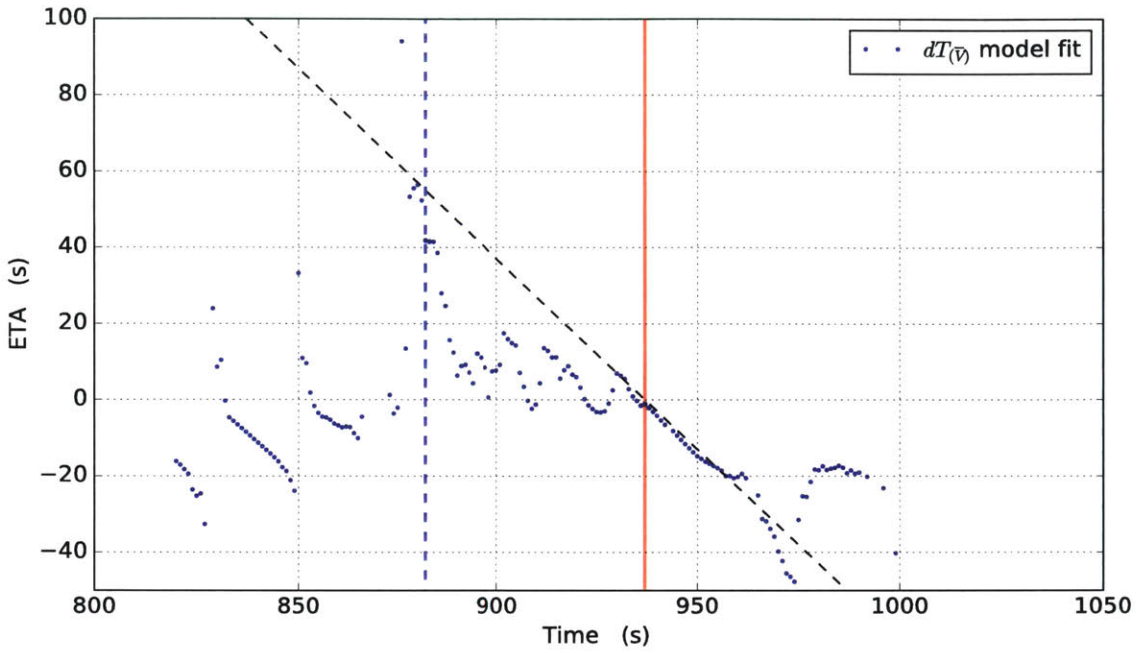

Figure 5-17: Intercept time estimates based on model fit of average RMS voltage $\overline{V}$, using a 20-point observation window. Variable path case study.

level, causing a drop in amplitude and likewise delaying the intercept time.

To further expand on possible changes along the travel path, the cases shown in Fig. 5-12 and Fig. 5-16 may be compared. The local maxima in the latter translated to significant shifts in the intercept time prediction and is reasonably explained by the scenarios described above. The former exhibits a similar behavior around its local maximum, where the measurements reflect a change in the approaching ship. Consider, for this purpose, the separation between the projected intercept time and the maximum measurements as was previously shown in Fig. 5-11, compared with the width of the valley around $t = 410$s.

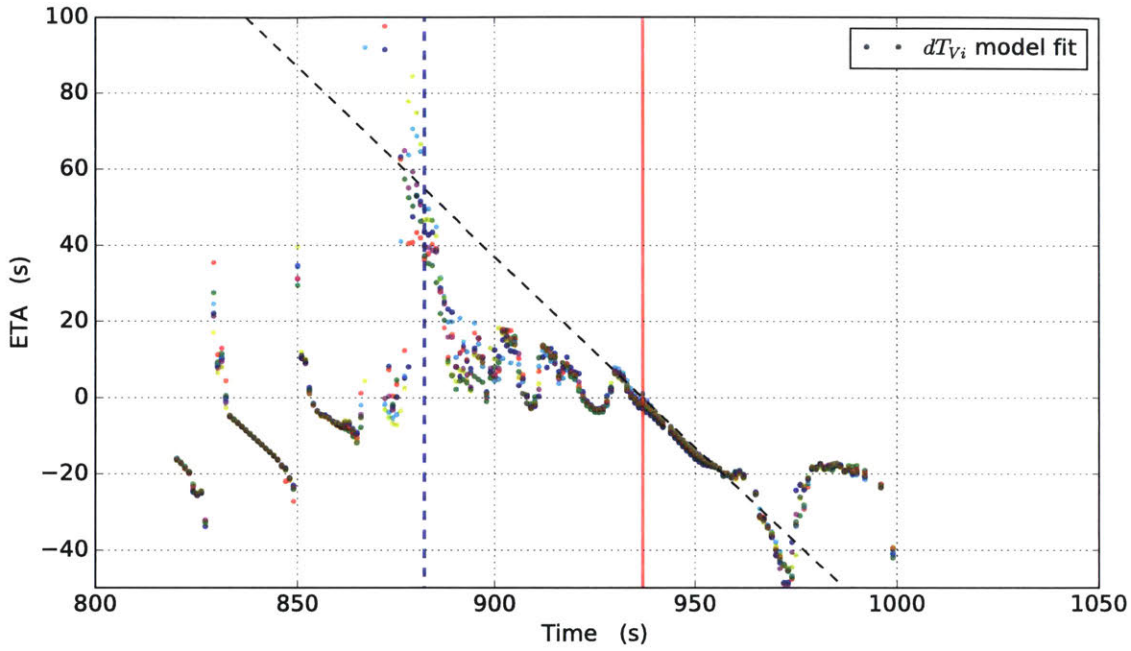

Figure 5-18: Intercept time estimates based on model fit of V_i, the RMS voltage per channel. Variable path case study.

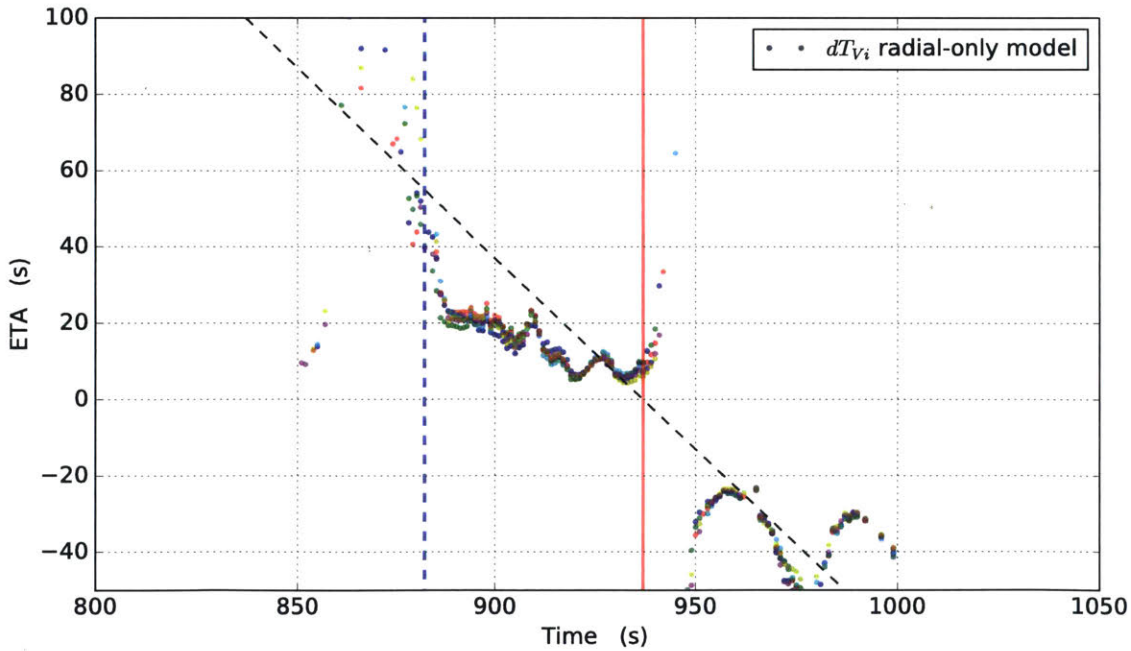

Figure 5-19: Intercept time estimates based on radial-only model fit of V_i, the RMS voltage per channel. Variable path case study.

5.3 Vehicle Array Data Processing

Understanding the limitations and responsiveness of the various estimation methods, as well as some of the more likely scenarios to be encountered by the AUV during deployment, is necessary in order to assemble a decision scheme for autonomous missions. Determining when a prediction is reliable and should be acted upon is the first step in the process of autonomous operation, followed by the determination of what may constitute an appropriate response. While there are many complex situations that may be of interest in the field, the AUV deployment tests performed for this work parted from the bimodal scenario described in Section 4.2.3 as a foundational framework to assess the ability of the AUV's systems to respond to an incoming vessel based solely on this passive acoustic detection system.

Given the incremental approach undertaken throughout this work, and the limitations imposed upon field work by seasonal conditions, the vehicle deployment experiments were performed between Summer and late Fall of 2016. The code implemented on the SandShark AUV during the test missions was based on the running-average approach. Decisions were triggered based on three key conditions, which could be adjusted for each distinct mission. First, the estimated intercept time should be below a configurable threshold, to avoid triggering on minimal-risk conditions. Second, the standard deviation of the predictions, projected to global time, should also remain below an adjustable limit to avoid triggering to random background noise. The third condition stemmed from the availability of a 4-element array onboard the vehicle, and the fact that the sensors may occasionally be subject to measurement spikes due to electronic as well as external factors. Thus, the last requirement was that a minimum of three out of the four channels have approximately equal time estimates.

Numerous preliminary tests were performed with the AUV and the line array, leading to a final experiment series to validate the vehicle's behavioral response. This last set consisted of six 20-30min deployments in the Charles River Basin, using loiter and racetrack path-based behaviors. A motorboat was used as the noise source, and was driven on approximately linear paths spanning a distance of approximately 400m,

from the western end of the Charles River Yacht Club towards the Harvard bridge. The short length of the travel path used meant that the time between throttle start and the closest point of approach - as recorded onboard the motorboat by visual contact - was less than 60s, giving the vehicle only a limited set of measurements to predict an intercept time and respond to the threat.

5.3.1 Behavior Triggering Case Study

The dataset shown in Fig. 5-20 corresponds to the second deployment performed on October 31, 2016, as part of the behavior-triggering experiments. The set contains three alarm triggers recorded on the AUV mission logs, at times $t = [284, 532, 919]$s. Fig. 5-21 shows the second event in the data set, where the moment of behavior switching marked by the green dashed line. It may be observed that the first 50s of the set are generally dominated by background noise. After maneuvering to align with the travel lane, the motorboat began its approach after the 500s mark. Following the approach introduced in earlier sections, Figs. 5-22 through 5-27 show the measurement gradients and dT estimates for the point-to-point and running average methods.

In Fig. 5-27, the clustering behavior of the intercept time estimates indicates a divergence from the linear path of approach. Indeed, as was discussed in Section 5.2, a variable path may affect the relative velocity vector, inducing changes in the trends observed for the dT estimates. A nearly constant guess for the time to arrival correlates with a nearly constant rate of change for the intensity measurements. Considering the surface shown in Fig. 3-1, this would correspond to a type of spiraling approach, which stands as a reasonable description of the test conditions given that the AUV's base mission is to hold a loiter path. After the SandShark triggers the alarm and switches to a racetrack behavior, the vessels' motion starts looking more like a linear path of approach and, accordingly, the intercept time estimates ultimately appear to converge towards a unit-slope linear relation. The effect of the singularity, as discussed in Section 3, can be clearly seen in the divergence of dT near the red line indicative of the measurement peak.

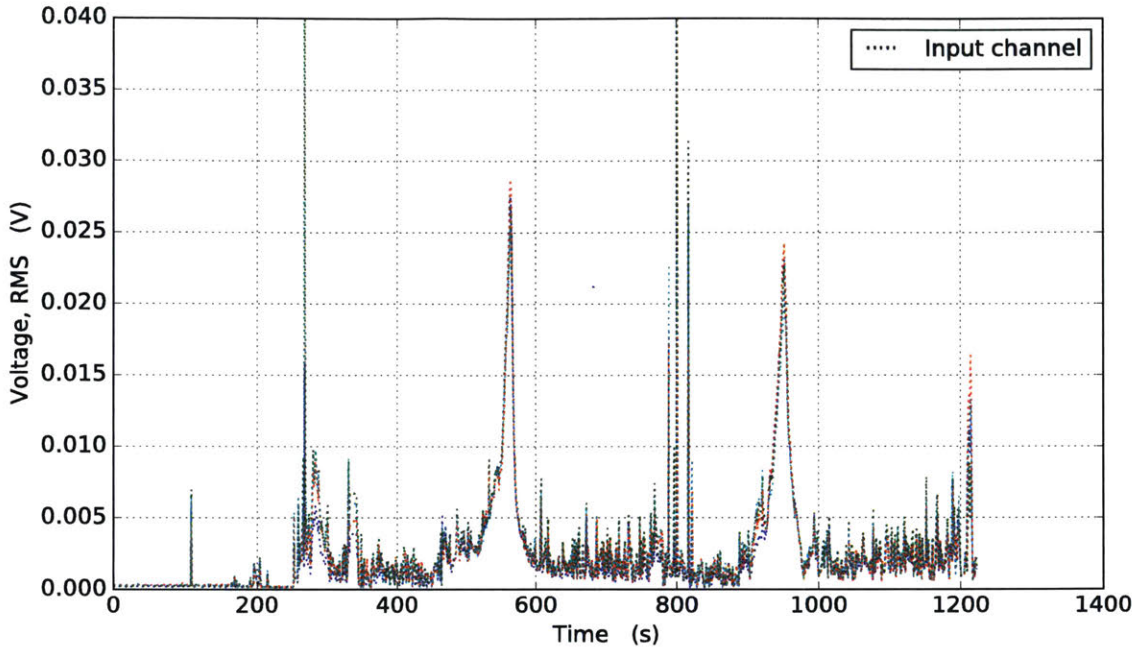

Figure 5-20: RMS of hydrophone voltage measurements collected with a 4-ch tetrahedral array mounted on a Bluefin SandShark AUV, during a 20-min mission on Oct. 31, 2016.

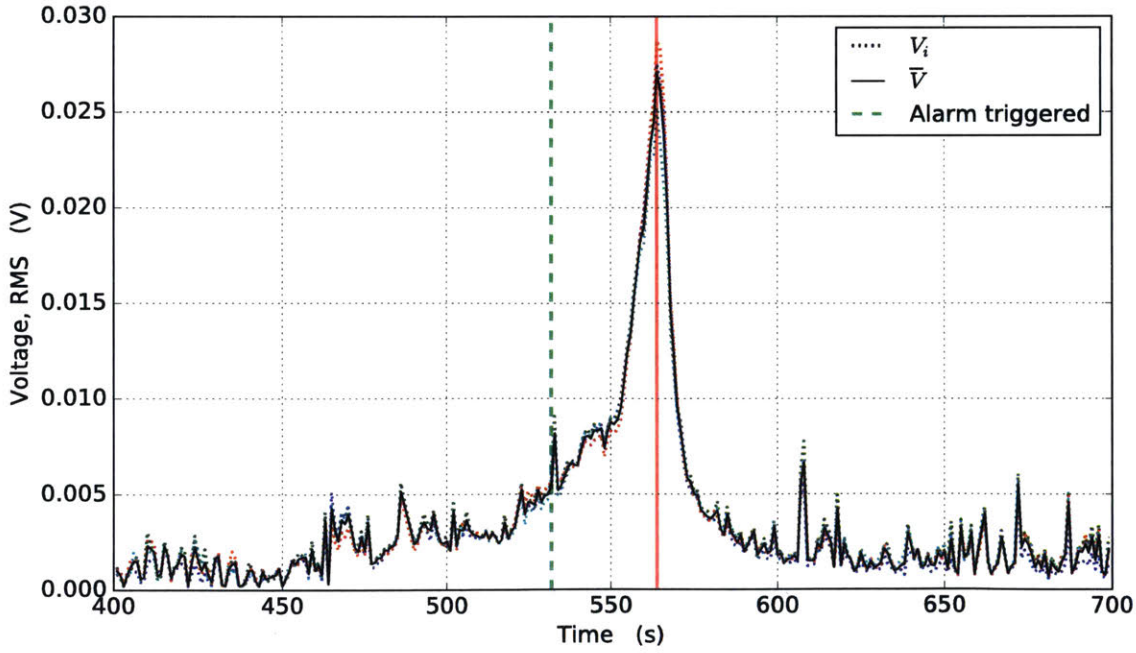

Figure 5-21: RMS of hydrophone voltage measurements collected with a 4-ch tetrahedral array mounted on a Bluefin SandShark AUV. Single event case study. Vehicle's intercept alarm triggered at time shown by green dashed line.

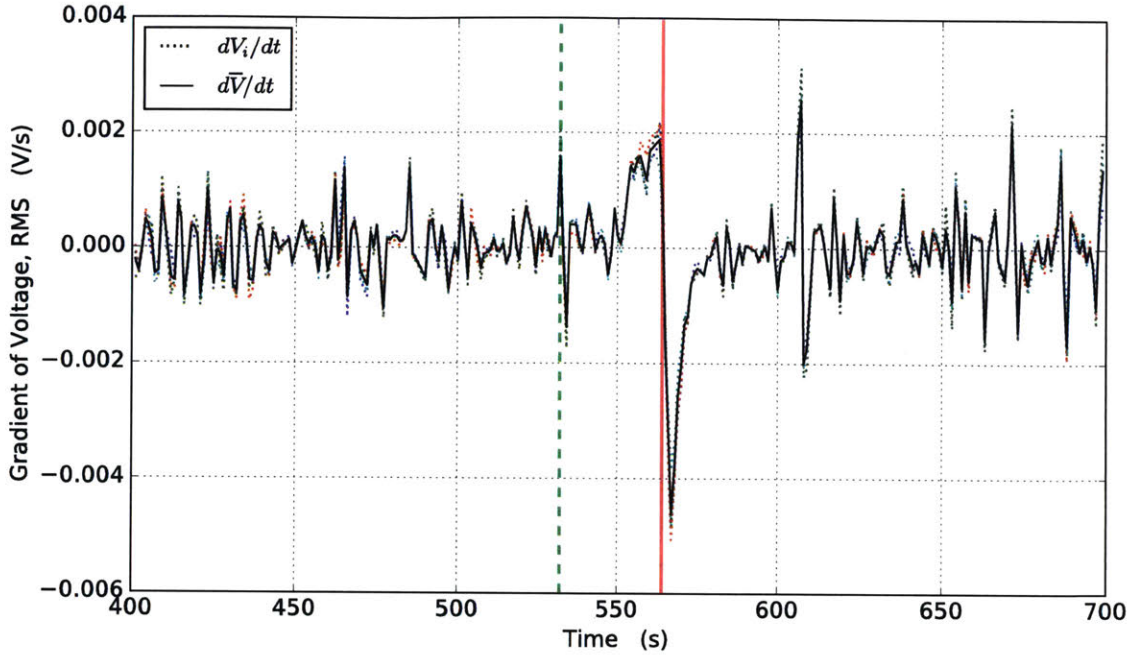

Figure 5-22: Gradient of RMS voltage measurements collected in the Charles River Basin with a 4-ch tetrahedral array mounted on a Bluefin SandShark AUV.

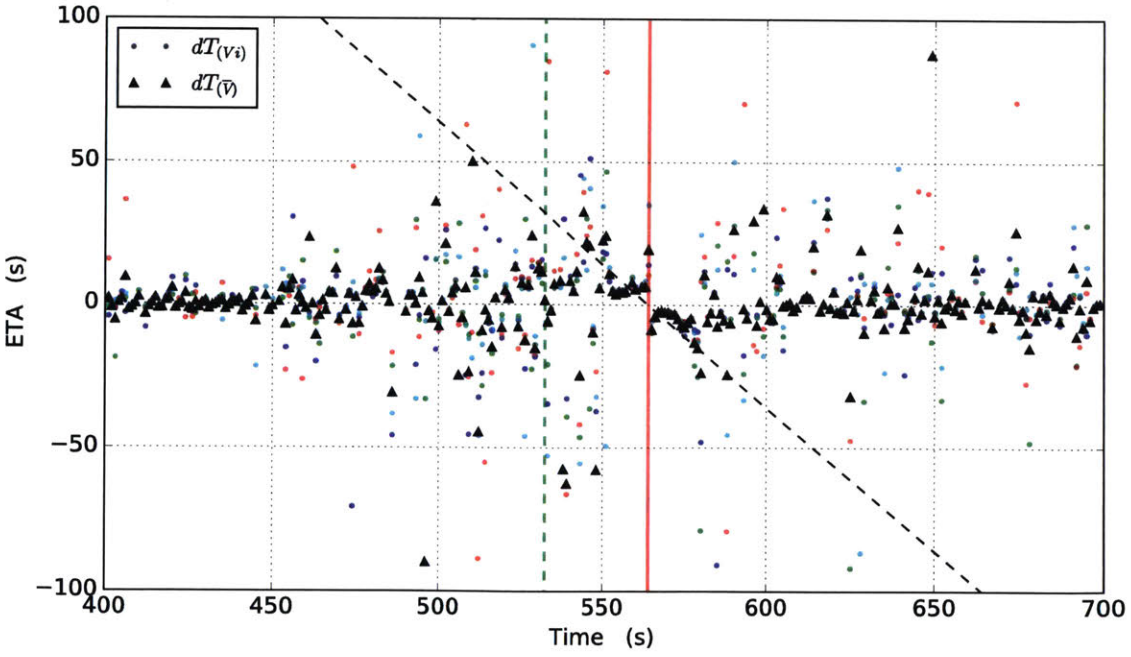

Figure 5-23: Intercept time estimates based on point-to-point gradient of RMS voltage.

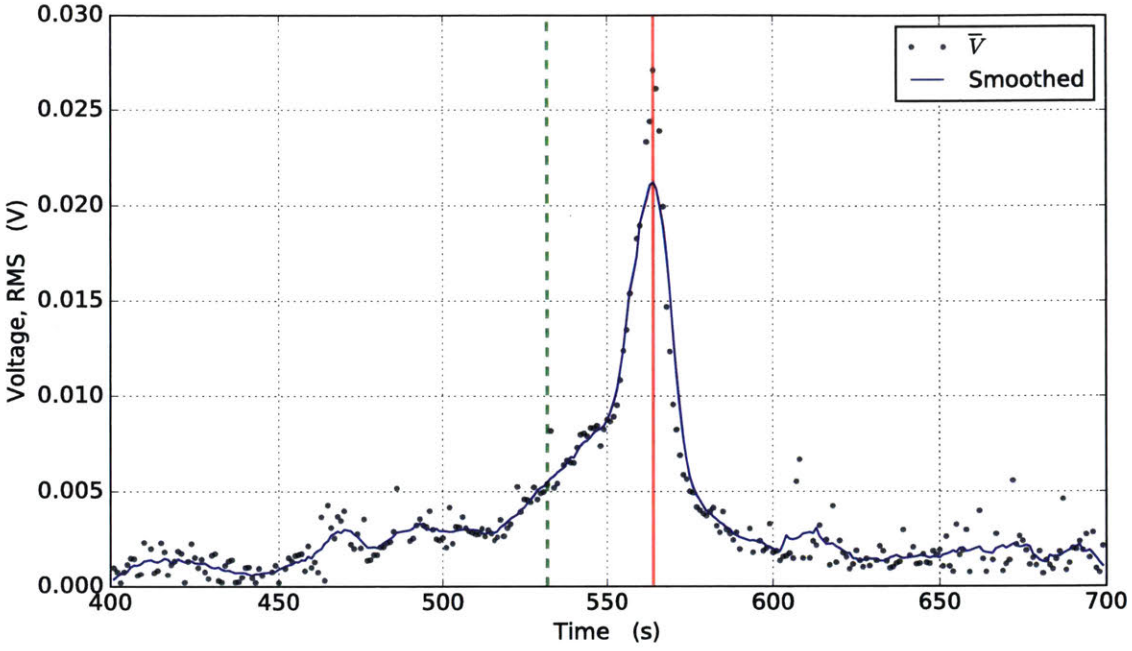

Figure 5-24: RMS of hydrophone voltage measurements, using a 10-point running-average smoothing window. Data shown obtained by post-processing of acoustic logs.

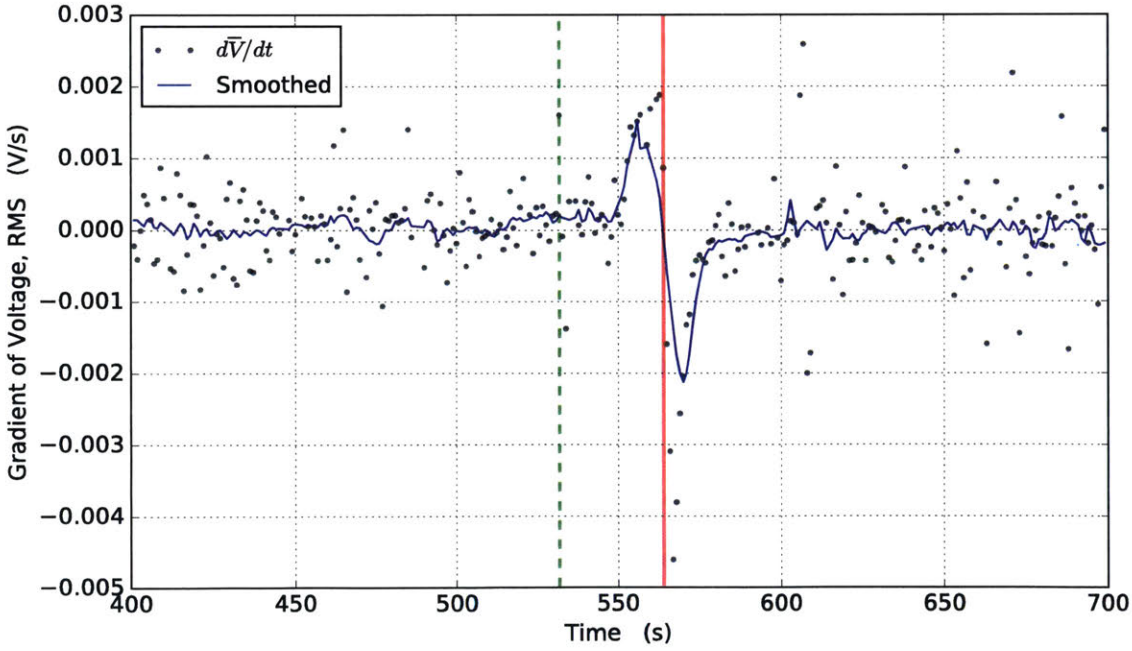

Figure 5-25: Gradient of RMS voltage measurements, using a 10-point running-average smoothing window.

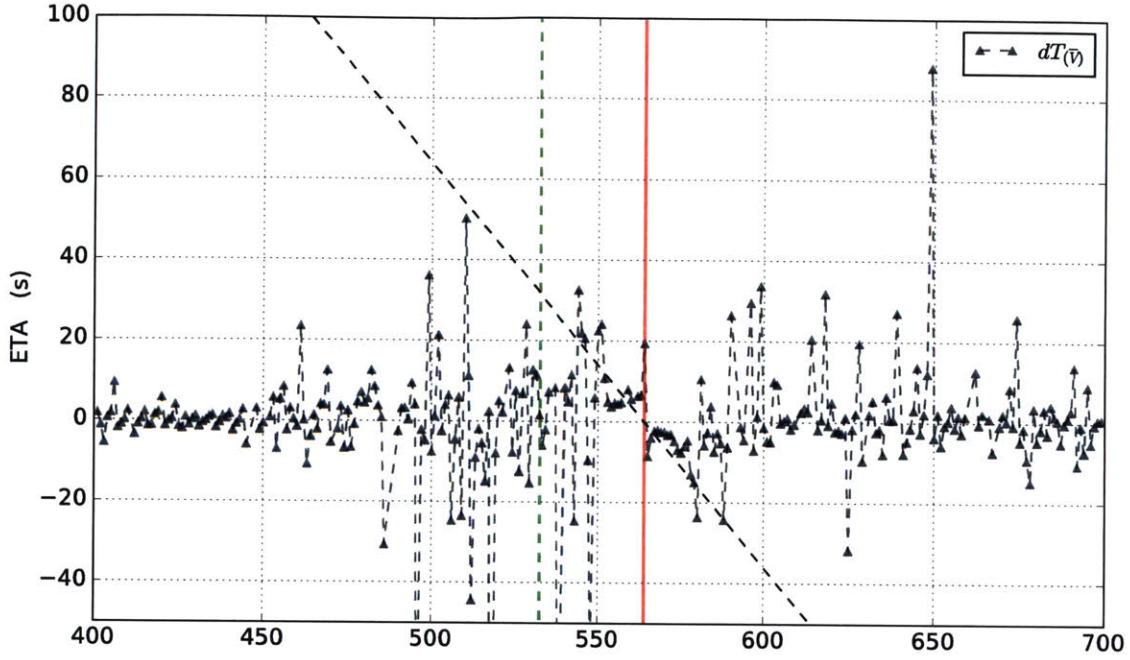

Figure 5-26: Intercept time estimates based on point-to-point gradient of RMS voltage.

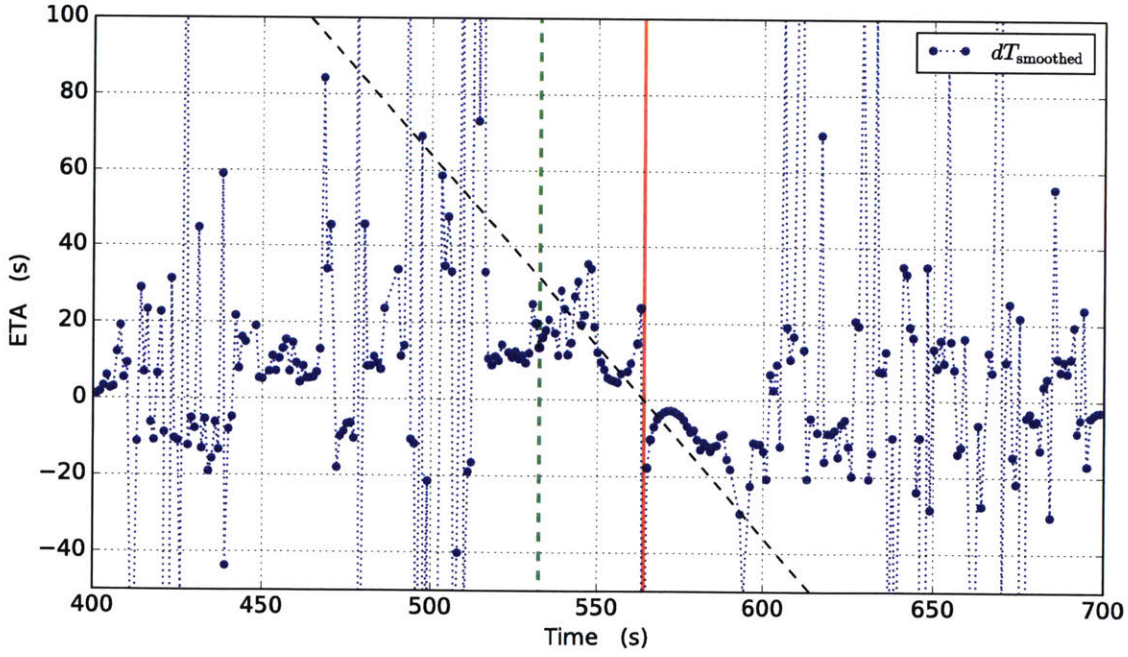

Figure 5-27: Intercept time estimates based on smoothed gradient of RMS voltage, using a 10-point running-average of the measurements.

The effect that a spiraling approach has on the measurements collected, in addition to the noise in the signal, provides an excellent opportunity to evaluate the limitations of the Lorentzian model curve-fitting routine. Because the data is much more linear, the fully described single-peak model has difficulty adapting with new measurements, and instead tends to lock on outliers and local maxima when present. This behavior can be seen in Figs. 5-28 through 5-31. However, by constraining the model to a radial-only form, disallowing any offset from the singularity, the curve-fitting routine begins to better match the running-average results. In Fig. 5-32, the reduced model function exhibits similar trends to those seen in Fig. 5-27, with a number of roughly constant measurements clustered to the left of the alarm marker, then shifting upwards and following the unit-slope line.

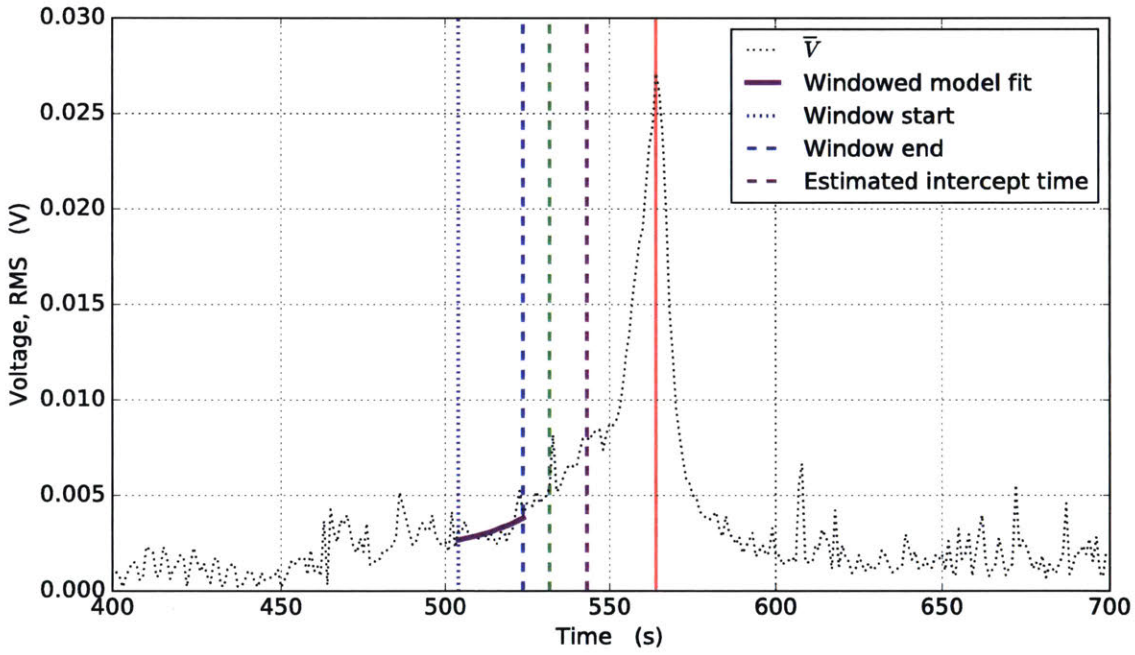

Figure 5-28: Overlay of an observation window fed to a curve-fitting routine, and the extended time-series of RMS voltage measurements. Actual peak (red) and estimated intercept time (magenta, dashed) shown. Vehicle's alarm trigger time (green, dashed) also shown.

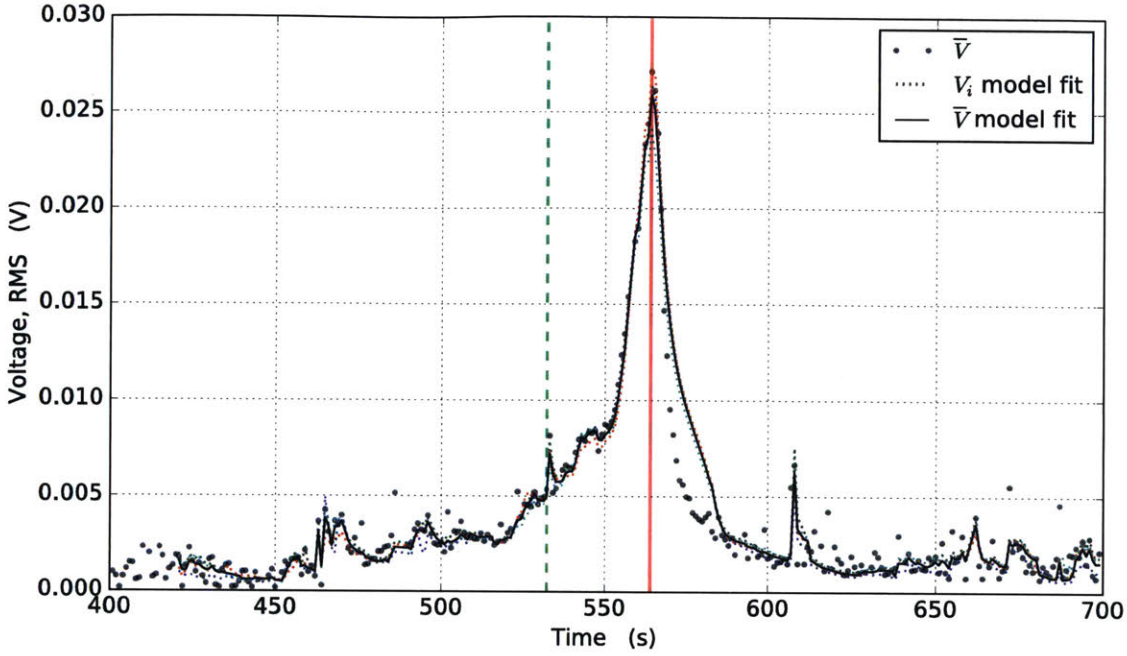

Figure 5-29: RMS voltage based on curve-fitting model with a 20-point observation window. Fit per channel and fit to average measurement $\overline{V}$ shown.

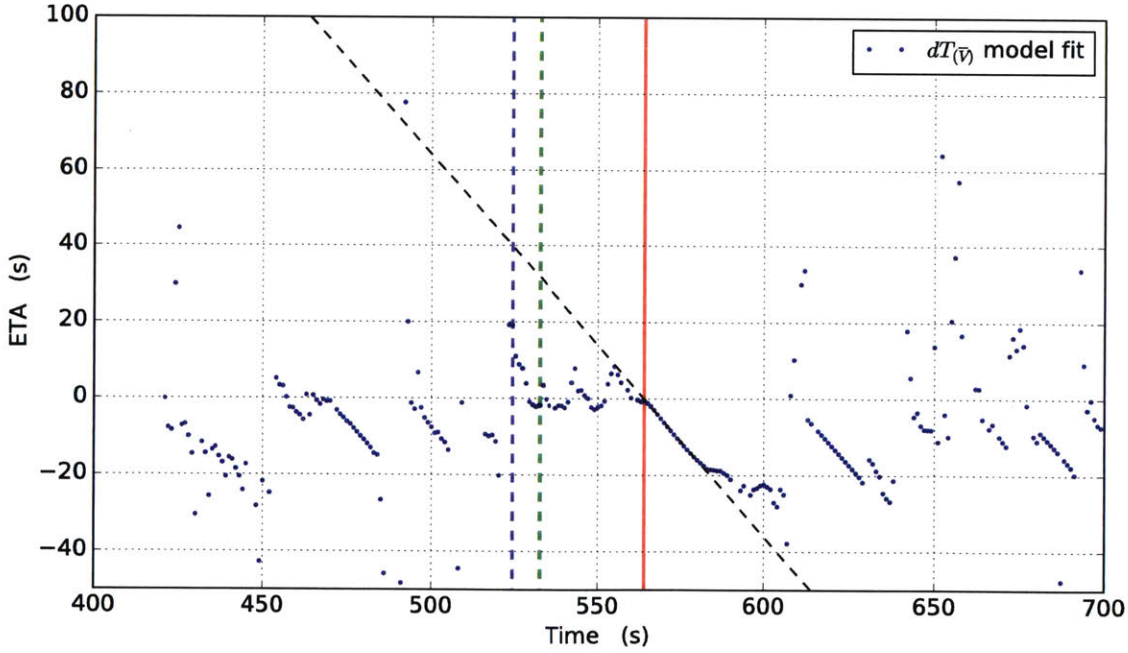

Figure 5-30: Intercept time estimates based on model fit of average RMS voltage $\overline{V}$, using a 20-point observation window.

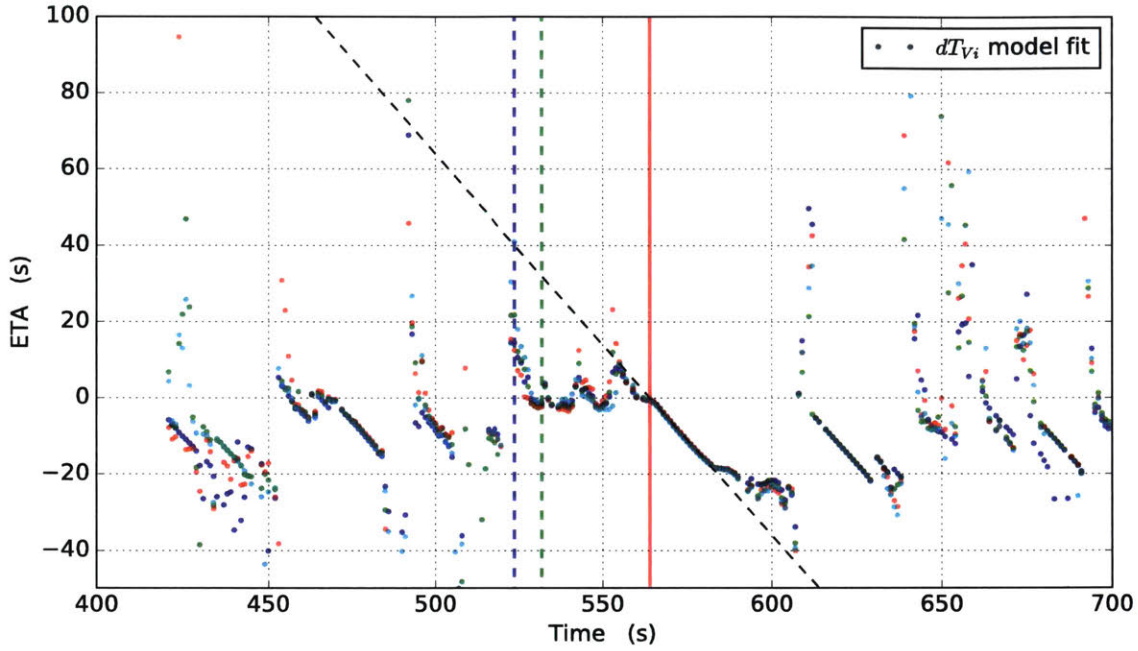

Figure 5-31: Intercept time estimates based on model fit of V_i, the RMS voltage per channel.

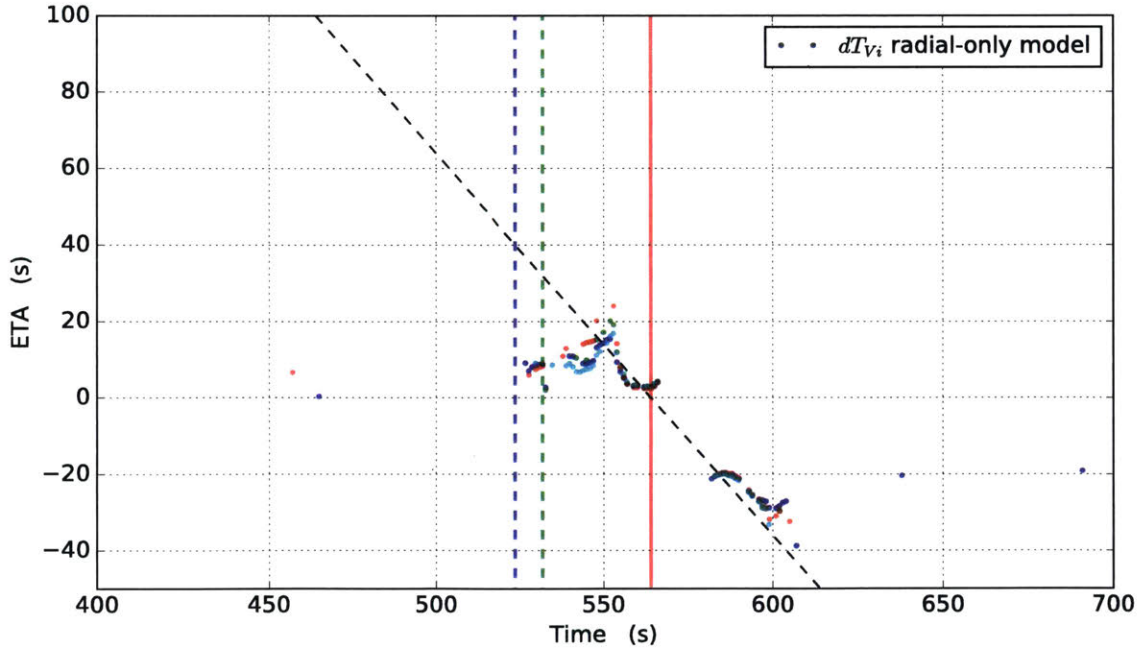

Figure 5-32: Intercept time estimates based on radial-only model fit of V_i, the RMS voltage per channel.

6 Conclusions

The deployment of a new sensor system or signal processing method for autonomous vehicles demands, by its very nature, that a significant series of testing be performed to validate the system's performance. Accounting for every possible situation is very nearly impossible, but by performing an increasing number of tests, a foundational decision scheme may be devised and improved upon. Throughout this work, a sequence of experiments was used to understand the principal aspects of the acoustic profiles observed in real operations areas, building up to onboard intercept time estimation. Numerous AUV deployments were performed in order to demonstrate fully autonomous responses to approaching threats based on the passive detection system herein presented. The final set of experiments consisted of six behavior-triggering tests with durations between 20-30min each, adding up to 142 minutes of acoustic data where a total of 21 successful response triggers were recorded.

The datasets collected throughout the different experimental stages were post-processed to assess the system performance and the validity of various estimation methods. A running average approach was compared with a fully described single-peak function and a reduced-form of the same function, constrained to direct radial approaches. This comparison shed some light on the effect of ambient noise, travel path variations and boundary reflections on the various estimates, thereby remarking the limitations of each method and the advantages attainable from using a parallel multi-model approach. The running-average method is subject to delays and peak damping, while the single-peak curve fit tends to fix on local peaks, often yielding unclear results during spiraling approaches; the radial function chosen exhibited a tendency to diverge when the measurement peaks were passing through the observation window. Furthermore, the effect of extreme outliers throughout the dataset affected the stability of each estimation method in different ways. By considering the different estimates in unison, however, an accurate description of the system could be drawn.

7 Future Work

Having proved that the system can be successfully operated during an autonomous mission deployment, a number of opportunities for improvement have been identified.

7.1 Parallel-Model Estimation

Following the local-maximum tracking ability of the single-peak function fit as was discussed in Section 5, the different models could be used to determine the best solution. Going a step further, the models could be not just considered in parallel but also combined to achieve a higher-confidence estimate. An example of this multi-model cross-over would be accounting for the latest point of interest as given by the Lorentzian model, such that the intercept time corresponding to the local-maximum time can be projected forward from all solutions to determine whether a response is necessary, according to the risk sensitivity of the mission.

7.2 Earliest-Detection Assessment

The behavior-triggering experiments proved the ability of the intercept estimation system to help the AUV respond to incoming threats. However, the short length of the travel lanes used by the motorboat during AUV deployment tests limited the time available for the SandShark to respond. Additional experiments should be performed to characterize the earliest detection times attainable with this passive system.

7.3 Frequency Filtering & Outlier Detection

In order to preserve the generality of the algorithm, the estimation methods were tested based on the full set of measurements. However, the nature of the phenomena sought by this system is limited by the ship speed, and may be generally considered

to have a slow rate of change. This information may be used to identify and remove extreme outliers in the measurement, which can improve the system's performance and stability. Furthermore, if the characteristic frequencies of the ship or ships in the area are known, a band-pass filter may be used to constrain the signal and account for variations in the desired frequency range alone.

7.4 Beamforming & Bearing-Based Filtering

Tests and signal processing throughout this work have been based on the premise of a single-channel system, and extended to multichannel measurements by using a simple time-bucket averaging of all channels. However, using more detailed methods such as conventional or adaptive beamforming can help further improve the signal-to-noise ratio by weighting the signal with an appropriate array gain. Besides its advantages in noise reduction, the additional bearing information obtained can also be used to account for sources with known signatures, such as those used for acoustic localization systems, or to enable tracking of multiple sources. This type of method provides an optimal way to combine the measurements from multiple sensors when their spatial configuration is known, as tends to be the case for AUV's, and should therefore be prioritized and integrated in future efforts on this work.

Bibliography

[1] T. Bandyophadyay, L. Sarcione, and F.S. Hover. A simple reactive obstacle avoidance algorithm and its application in singapore harbor. In *Field and Service Robotics*, volume 62 of *Springer Tracts in Advanced Robotics*, pages 455–465. Springer Berlin Heidelberg, 2010.

[2] Bluefin Robotics. Bluefin SandShark. In *http://www.bluefinrobotics.com/vehicles-batteries-and-services/bluefin-sandshark/*, 2016. Accessed: 2016-06-18.

[3] F.B. Jensen, W.A. Kuperman, M.B. Porter, and H. Schmidt. *Computational Ocean Acoustics*. Springer, New York, NY (USA), 2nd edition, 2011.

[4] X. Jin and A. Ray. Navigation of autonomous vehicles for oil spill cleaning in dynamic and uncertain environments. *International Journal of Control*, 87(4):787–801, 2014.

[5] A.L. Kukulya, J.G. Bellingham, J.W. Kaeli, C.M. Reddy, M.A. Godin, and R.N. Conmy. Development of a propeller driven long range autonomous underwater vehicle (lrauv) for under-ice mapping of oil spills and environmental hazards: An arctic domain center of awareness project (adac). In *2016 IEEE/OES Autonomous Underwater Vehicles (AUV)*, pages 95–100. Institute of Electrical and Electronics Engineers (IEEE), Nov 2016.

[6] A.L. Kukulya, R. Stokey, and C. Fiester. Multi-vehicle autonomous tracking and filming of white sharks carcharodon carcharias. In *2016 IEEE/OES Autonomous Underwater Vehicles (AUV)*, pages 95–100. Institute of Electrical and Electronics Engineers (IEEE), Nov 2016.

[7] H. Kuttruff. *Acoustics: an introduction*. CRC Press, Boca Raton, FL (USA), 2006.

[8] R.W. Larson. Disruptive innovation and naval power : strategic and financial implications of unmanned underwater vehicles (uuvs) and long-term underwater power sources. Master's thesis, Massachusetts Institute of Technology, Feb 2014.

[9] M. Novitzky, H.R.R. Dougherty, and M.R. Benjamin. A human-robot speech interface for an autonomous marine teammate. In A. Agah, J.J. Cabibihan, A.M. Howard, M.A. Salichs, and H. He, editors, *Social Robotics: 8th International Conference, ICSR 2016, Kansas City, MO, USA, November 1-3, 2016 Proceedings*, pages 513–520, Cham, Nov 2016. Springer International Publishing.

[10] H. Schmidt and M.R. Benjamin. Autonomous Littoral Passive Acoustic Collision Alarm. Technical report, Laboratory for Autonomous Marine Sensing Systems, Massachusetts Institute of Technology, Cambridge, MA, June 2011.

[11] H. Schmidt and M.R. Benjamin. System and method for collision avoidance in underwater vehicles, Sep 2014. US Patent 8,830,793.

[12] O. A. Viquez, E. M. Fischell, N. R. Rypkema, and H. Schmidt. Design of a general autonomy payload for low-cost AUV R&D. In *2016 IEEE/OES Autonomous Underwater Vehicles (AUV)*, pages 151–155, Nov 2016.

[13] O.A. Viquez Rojas. Evaluation of an acoustic detection algorithm for reactive collision avoidance in underwater applications. Bachelor's thesis, Massachusetts Institute of Technology, June 2013.